



2019

## QUANTIFICATION OF MYOCARDIAL MECHANICS IN LEFT VENTRICLES UNDER INOTROPIC STIMULATION AND IN HEALTHY RIGHT VENTRICLES USING 3D DENSE CMR

Zhan-Qiu Liu

University of Kentucky, lafeir.lew@gmail.com

Digital Object Identifier: <https://doi.org/10.13023/etd.2019.043>

[Right click to open a feedback form in a new tab to let us know how this document benefits you.](#)

---

### Recommended Citation

Liu, Zhan-Qiu, "QUANTIFICATION OF MYOCARDIAL MECHANICS IN LEFT VENTRICLES UNDER INOTROPIC STIMULATION AND IN HEALTHY RIGHT VENTRICLES USING 3D DENSE CMR" (2019). *Theses and Dissertations--Mechanical Engineering*. 130.

[https://uknowledge.uky.edu/me\\_etds/130](https://uknowledge.uky.edu/me_etds/130)

This Doctoral Dissertation is brought to you for free and open access by the Mechanical Engineering at UKnowledge. It has been accepted for inclusion in Theses and Dissertations--Mechanical Engineering by an authorized administrator of UKnowledge. For more information, please contact [UKnowledge@lsv.uky.edu](mailto:UKnowledge@lsv.uky.edu).

## **STUDENT AGREEMENT:**

I represent that my thesis or dissertation and abstract are my original work. Proper attribution has been given to all outside sources. I understand that I am solely responsible for obtaining any needed copyright permissions. I have obtained needed written permission statement(s) from the owner(s) of each third-party copyrighted matter to be included in my work, allowing electronic distribution (if such use is not permitted by the fair use doctrine) which will be submitted to UKnowledge as Additional File.

I hereby grant to The University of Kentucky and its agents the irrevocable, non-exclusive, and royalty-free license to archive and make accessible my work in whole or in part in all forms of media, now or hereafter known. I agree that the document mentioned above may be made available immediately for worldwide access unless an embargo applies.

I retain all other ownership rights to the copyright of my work. I also retain the right to use in future works (such as articles or books) all or part of my work. I understand that I am free to register the copyright to my work.

## **REVIEW, APPROVAL AND ACCEPTANCE**

The document mentioned above has been reviewed and accepted by the student's advisor, on behalf of the advisory committee, and by the Director of Graduate Studies (DGS), on behalf of the program; we verify that this is the final, approved version of the student's thesis including all changes required by the advisory committee. The undersigned agree to abide by the statements above.

Zhan-Qiu Liu, Student

Dr. Jonathan F. Wenk, Major Professor

Dr. Alexandre Martin, Director of Graduate Studies

QUANTIFICATION OF MYOCARDIAL MECHANICS IN LEFT VENTRICLES  
UNDER INOTROPIC STIMULATION AND IN HEALTHY RIGHT VENTRICLES  
USING 3D DENSE CMR

---

DISSERTATION

---

A dissertation submitted in partial fulfillment of the requirements for the degree of  
Doctor of Philosophy in the College of Engineering at the University of Kentucky

By

Zhan-Qiu Liu

Lexington, Kentucky

Director: Dr. Jonathan F. Wenk, Professor of Mechanical Engineering

Lexington, Kentucky

2018

Copyright © Zhan-Qiu Liu 2018

## ABSTRACT OF DISSERTATION

### QUANTIFICATION OF MYOCARDIAL MECHANICS IN LEFT VENTRICLES UNDER INOTROPIC STIMULATION AND IN HEALTHY RIGHT VENTRICLES USING 3D DENSE CMR

Statistical data from clinical studies indicate that the death rate caused by heart disease has decreased due to an increased use of evidence-based medical therapies. This includes the use of magnetic resonance imaging (MRI), which is one of the most common non-invasive approaches in evidence-based health care research. In the current work, I present 3D Lagrangian strains and torsion in the left ventricle of healthy and isoproterenol-stimulated rats, which were investigated using Displacement ENcoding with Stimulated Echoes (DENSE) cardiac magnetic resonance (CMR) imaging. With the implementation of the 12-segment model, a detailed profile of regional cardiac mechanics was reconstructed for each subject. Statistical analysis revealed that isoproterenol induced a significant change in the strains and torsion in certain regions at the mid-ventricle level. In addition, I investigated right ventricular cardiac mechanics with the methodologies developed for the left ventricle. This included a comparison of different regions within the basal and mid-ventricular regions. Despite no regional variation found in the peak circumferential strain, the peak longitudinal strain exhibited regional variation at the anterior side of the RV due to the differences in biventricular torsion, mechanism of RV free wall contraction, and fiber architecture at RV insertions. Future applications of the experimental work presented here include the construction and validation of biventricular finite element models. Specifically, the strains predicted by the models will be statistically compared with experimental strains. In addition, the results of the present study provide an essential reference of RV baseline evaluated with DENSE MRI, a highly objective technique.

KEYWORDS: Biventricular, Right Ventricle, DENSE MRI, 3D Lagrangian Strains, Rats, 3D DENSE Plugin for Crescent Organ

---

Zhan-Qiu Liu

---

11/01/2018

---

QUANTIFICATION OF MYOCARDIAL MECHANICS IN LEFT VENTRICLES  
UNDER INOTROPIC STIMULATION AND IN HEALTHY RIGHT VENTRICLES  
USING 3D DENSE CMR

By

Zhan-Qiu Liu

---

Jonathan F. Wenk

Director of Dissertation

---

Alexandre Martin

Director of Graduate Studies

---

11/29/2018

---

## ACKNOWLEDGMENTS

Though an individual work, the following dissertation would not have been possible without the help and support of many people.

First of all, I would love to express my genuine gratitude to my supervisor, Dr. Jonathan F. Wenk, for tutoring and enlightening me over the years, for his offer of academic freedom, for sparking my thinking, for his patience with my crazy ideas, and for his respect for my decision.

In addition, I am truly grateful to Dr. David Powell for generously giving me so much of his time, to offer me insights about MRI, and to timely provide me with instructive comments about my questions.

Thank you to Mrs. Beverly Meacham who offered me so much help and instruction on animal experiments.

Next, I wish to thank my dissertation committee members: Dr. Martha Grady, Dr. Keith Rouch, and Dr. Kenneth Campbell. Thank you for taking time to participate in my thesis defense. Thank you to Dr. Laurence Hassebrook for serving as the outside examiner in my defense.

Rat preparation and DENSE MRI acquisition were done by Dr. Xiaoyan Zhang and I would particularly like to thank her for producing wonderful images. Thank you to Amir Nikou and Dara Singh for their help.

Last but not least, a huge hug to my amazing parents. Without their unconditional support and encouragement, I would not have been able to handle all of the ups and downs. I cannot thank them enough.

It's sad I will leave them soon and cannot work and live around these people in a short term. But it's time to move on!

## TABLE OF CONTENTS

ACKNOWLEDGMENTS .....	iii
TABLE OF CONTENTS .....	iv
LIST OF TABLES .....	vi
LIST OF FIGURES .....	vii
1 Introduction.....	1
1.1 Motivation.....	1
1.2 Anatomy of the Heart.....	1
1.3 Physiology of the Heart.....	4
1.4 Segmentation of the Heart.....	8
1.5 Cine Displacement ENcoding with Stimulated Echoes (DENSE) MRI.....	11
1.6 Computing Mechanics .....	17
2 Quantification of 3D Lagrangian Strain and Torsion in Rat Left Ventricles under Inotropic Stimulation using 3D cine DENSE MRI.....	21
2.1 Background .....	21
2.2 Methods.....	22
2.2.1 Myocardial Segmentation .....	22
2.2.2 Discretization of the LV in the Referential Frame .....	28
2.2.3 Segmentation of the LV Mid-ventricle .....	31
2.2.4 Statistical Analysis .....	32
2.3 Results.....	32
2.3.1 Global Function of LV .....	32
2.3.2 Regional Differences of Peak Circumferential Strain in the LV Mid-ventricle	35
2.4 Comparison between 2D and 3D Strain Analysis .....	37
2.5 Conclusion .....	41
3 Quantification of Regional Right Ventricular Strain in Healthy Rats using 3D Spiral Cine DENSE MRI.....	43
3.1 Background .....	43
3.2 Methods.....	46
3.2.1 Myocardial Segmentation .....	46

3.2.2	3D Anatomical Contours.....	48
3.2.3	Discretization of Biventricular Surfaces .....	51
3.2.4	Lagrangian Strains Analysis .....	54
3.2.5	Statistical Analysis .....	58
3.3	Result .....	58
3.3.1	Distribution of Peak Systolic Strains at Base and Mid-ventricle of RV .....	58
3.3.2	Distribution of Peak Systolic Strains in the RV Base .....	59
3.3.3	Distribution of Peak Systolic Strains in the RV Mid-ventricle .....	60
3.4	Discussion .....	61
3.5	Limitations .....	66
3.6	Conclusion .....	67
3.7	Clinical Implications .....	68
	Appendices.....	69
	Appendix A – Abbreviations .....	69
	References .....	70
	Vita .....	77



## LIST OF TABLES

Table 1.1: Phases and stages of cardiac cycle .....	5
Table 2.1: Notation of LV mid-ventricular segments.....	31
Table 2.2: Hemodynamic parameters in baseline and isoproterenol-infused rats.....	33
Table 2.3: Effects of isoproterenol on the global peak Lagrangian strains and circumferential-longitudinal shear angles in basal, mid-ventricular, and apical region of the LV. * $p < 0.05$ . (Zhang et al., 2018) .....	34
Table 3.1: Notation of segments in RV free wall .....	57

## LIST OF FIGURES

Figure 1.1: Structure Diagram of the human heart from an anterior section (en.wikipedia.org/wiki/Ventricle_(heart)).....	2
Figure 1.2: Heart location from an anterior view of human body (Prentice Hall, 2016)....	3
Figure 1.3: Layers of the heart wall (en.wikipedia.org/wiki/Endocardium).....	4
Figure 1.4: Wiggers Diagram of a cardiac cycle (en.wikipedia.org/wiki/File:Wiggers_Diagram.png) .....	5
Figure 1.5: Schematic of blood circulation with red arrows as oxygenated blood and blue arrows as deoxygenated blood .....	7
Figure 1.6: Pressure volume loop of a typical human cardiac cycle (Center for Teaching and Learning in Columbia, 2016) .....	7
Figure 1.7: Definitions of short axis (SA), vertical long-axis (VLA), and horizontal long-axis (HLA) views (Cerqueira, 2002).....	8
Figure 1.8: Schematic of segmentation of left ventricle (Cerqueira, 2002).....	9
Figure 1.9: Assignment of the myocardial segments to specific coronary artery territories (Cerqueira, 2002) .....	10
Figure 1.10: Coronary arteries and major veins of the heart (Sky, 2017).....	10
Figure 1.11: DENSE pulse sequence and representative outputs of DENSE acquisition .	11
Figure 1.12: Timing diagram for the 3D cine DENSE spiral pulse sequence (Faro and Mohamed, 2006) .....	13
Figure 1.13: Diagram of k-space trajectories covered over a field-of-view (Meyer, 1998) .....	13
Figure 1.14: Four weighting vectors for 3D balanced multi-point encoding method (Zhong et al., 2009).....	16
Figure 1.15: Striping Artifacts caused by bright blood signal (Aletras et al., 1999) .....	17
Figure 1.16: Left ventricular volumetric meshes. $60 \times 3 \times 4$ elements were built in circumferential, transmural and longitudinal directions reconstructed from the MRI images scanned on Aug. 30, 2015. An 8-noded brick element is in an arbitrary location of the mesh .....	17
Figure 1.17: Transformation from Cartesian coordinates to polar coordinates .....	18
Figure 1.18: Definition of torsion T between basal and apical slices (Rüssel et al., 2009) .....	20
Figure 2.1: Left ventricular contours at isoproterenol-simulated end diastole of mid-ventricle. Images were taken on Feb. 27, 2016. Red curves are epicardial contours. Green curves are LV endocardial contours. Yellow curves are RV endocardial contours. ....	24
Figure 2.2: Papillary muscles in human heart (criticalecho.com) .....	25
Figure 2.3: Exclusion of papillary muscle from myocardial contours .....	27
Figure 2.4: Meshing user interface for a short-axis slice .....	29
Figure 2.5: A 12-segment model at mid ventricle .....	32

Figure 2.6: Effects of isoproterenol on peak systolic  $E_{cc}$  strains in different myocardial regions of mid-ventricle. Peak systolic  $E_{cc}$  values were averaged over each segment of sub-endocardium (A, Endo), mid-myocardium (B, Mid), and sub-epicardium (C, Epi). The text above each figure shows p values for the main statistical effects. Significant differences between CTL and ISO groups, tested separately for each segment, are indicated by asterisks (\* $p < 0.05$ ). Significant differences among the four segments, tested separately for untreated (CTL) and isoproterenol-treated (ISO) rats, are listed in the inset box. (Zhang et al., 2018)

.....	36
Figure 2.7: Comparison in $E_{cc}$ between 2D and 3D Strain Analysis .....	39
Figure 2.8: Effect of isoproterenol on peak deformation gradient shear component $F_{lc}$ .	40
Figure 3.1: Biventricular contours at end diastole of mid-ventricle. Images were taken on Aug. 30, 2015. Red curves are epicardial contours. Green curves are LV endocardial contours. Yellow curves are RV endocardial contours.....	48
Figure 3.2: Converted end-diastolic contours of all slices are gathered in the global coordinate system. Blue curves are SA contours. Red curves are LA contours. Black curves are approximated SA contours. ....	50
Figure 3.3: An apical SA contour is approximated with the points in two LA contours. Red curve is the apical SA contour. Black points are from LA contours. ....	51
Figure 3.4: End-diastolic biventricular meshes created with DENSE3D Plugin .....	52
Figure 3.5: Refinement for end-diastolic RV endocardial mesh. Blue curves are a stack of converted end-diastolic SA contours. ....	53
Figure 3.6: End-diastolic biventricular meshes with a refined RV mesh.....	54
Figure 3.7: Biventricular longitudinal and circumferential segmentation .....	56
Figure 3.8: A 12-segment model at RV free wall.....	57
Figure 3.9: RV segmentation model in LA view (Hurst, 1988) .....	58
Figure 3.10: Distribution of peak systolic strains at base and mid-ventricle of RV .....	59
Figure 3.11: Distribution of Peak Systolic Strains in the RV Base .....	60
Figure 3.12: Distribution of Peak Systolic Strains in the RV mid-ventricle .....	61
Figure 3.13: Schematic of torsion direction as viewed from the apex. ....	64
Figure 3.14: Positive longitudinal strain values (black dots) found at end systole near the insertion of the rat RV scanned on Nov. 01, 2015. ....	65

# **1 Introduction**

## **1.1 Motivation**

Latest statistics from CDC WONDER online database indicate that heart disease was the most common cause of death for both men and women in the United States from 1999-2014 (CDC). The good news is that the death rate attributable to heart disease was decreased by 24% from 1999 to 2014 (CDC), and studies reveal that 47% of the decrease in US deaths caused by coronary heart disease was credited to the increasing use of evidence-based medical therapies from 1980 to 2000 (Ford et al., 2007). Among many approaches for evidence-based health care practices magnetic resonance imaging (MRI), which is a non-invasive technique, has become widely used and a gold standard in cardiovascular diagnostic therapies.

## **1.2 Anatomy of the Heart**

The basic anatomy of the heart is shown in Figure 1.1. There are four chambers in the heart, two large chambers known as ventricles and two smaller chambers known as atria. The wall separating the left and right ventricles is called the septum, while the rest part of wall is called free wall. The septum is convex toward the right ventricle (RV) during a cardiac cycle. In human hearts, the RV volume is larger than the left ventricle (LV) volume. There are also four important valves inside the heart. Two valves connecting the ventricles and the atria are termed atrioventricular (AV) valves. They are the mitral valve between

left ventricle and left atrium and the tricuspid valve between right ventricle and right atrium.

Another two valves connecting the ventricles and the arteries are termed semilunar valves.

Between the left ventricle and aorta is the aortic valve, while between the right ventricle and pulmonary artery is the pulmonic valve.

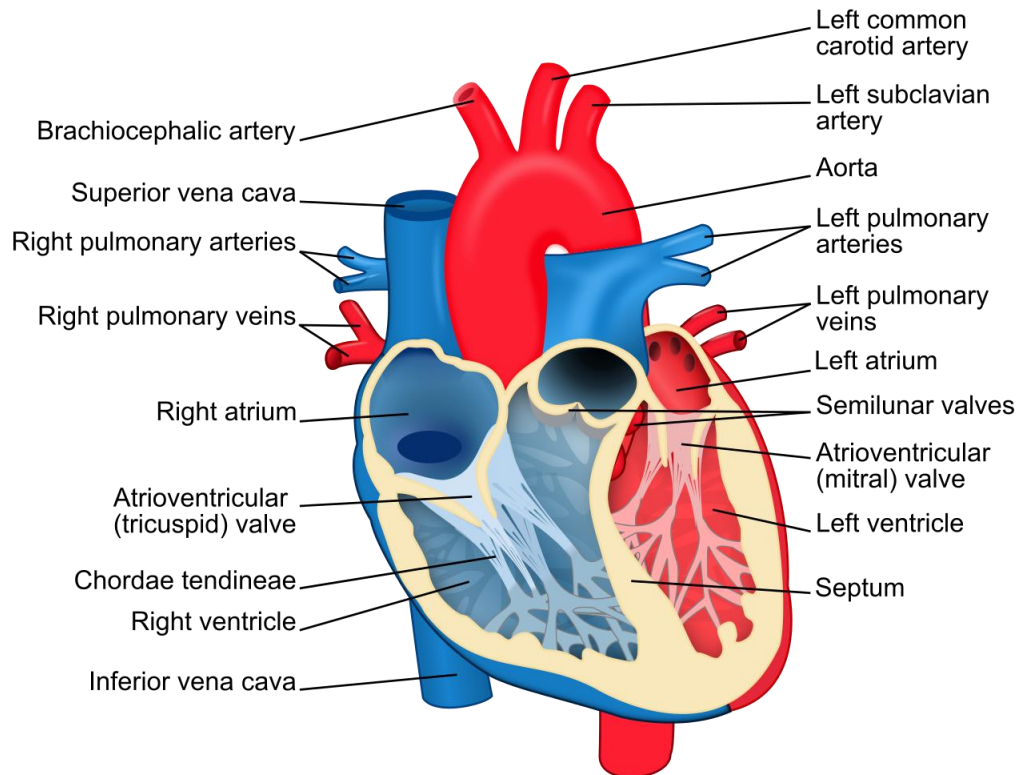


***Figure 1.1: Structure Diagram of the human heart from an anterior section***

*([en.wikipedia.org/wiki/Ventricle\\_\(heart\)](https://en.wikipedia.org/wiki/Ventricle_(heart)))*

The ventricles can be divided into the base, the middle cavity, and the apex along the longitudinal direction. The base of ventricles is the uppermost and widest part, where the right ventricle (RV) is attached to venae cavae and left pulmonary artery, and where the left ventricle (LV) is attached to aorta and left pulmonary veins. The apex of ventricles is the

lowest part. Their directions are shown in the anterior view of human body (Figure 1.2).

The base directs upward and pointing to the right shoulder, while the apex is downward, forward, and leaning toward the left shoulder.

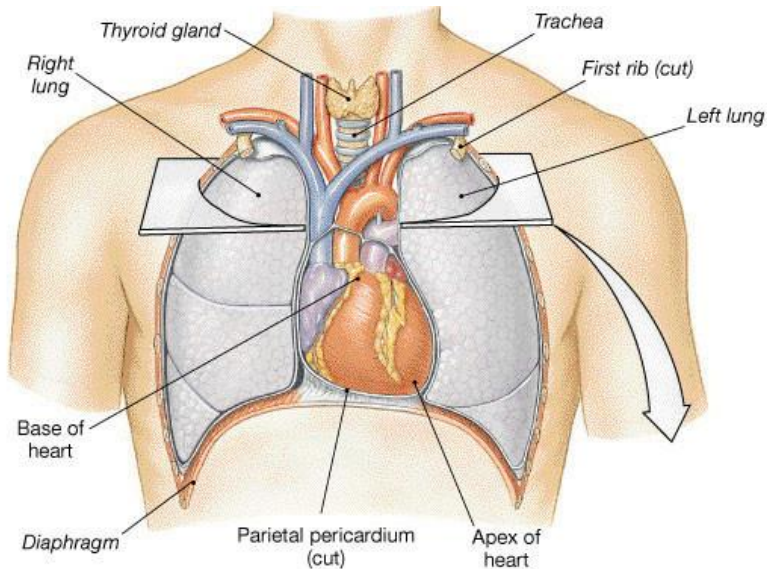


***Figure 1.2: Heart location from an anterior view of human body (Prentice Hall, 2016)***

There are three transmural layers in the ventricular wall (Figure 1.3). The endocardium is the innermost layer, while the epicardium is the outer layer of heart tissue. The myocardium is the majority of ventricular wall between endocardium and epicardium. The myocardium is composed of bundles of myofibers, organized into sheet-like structures, which are responsible for ventricular contraction. The angle of these fibers varies from near  $60^\circ$  at the endocardium to near  $-60^\circ$  at the epicardium, relative to the circumferential direction (Streeter et al., 1969).

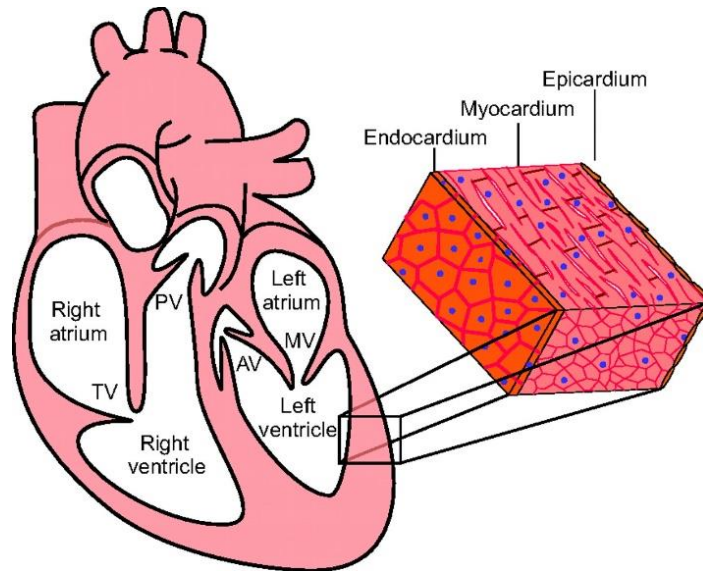


*Figure 1.3: Layers of the heart wall ([en.wikipedia.org/wiki/Endocardium](https://en.wikipedia.org/wiki/Endocardium))*

### 1.3 Physiology of the Heart

When the heart is beating, contraction and relaxation occur alternately, and each heartbeat is called one cardiac cycle (shown in Figure 1.4). Heart rate is used to describe the frequency of the heartbeat. The most common unit is beats per minute. A cardiac cycle can be divided into two phases, systole and diastole, or five stages (summarized in Table 1.1).

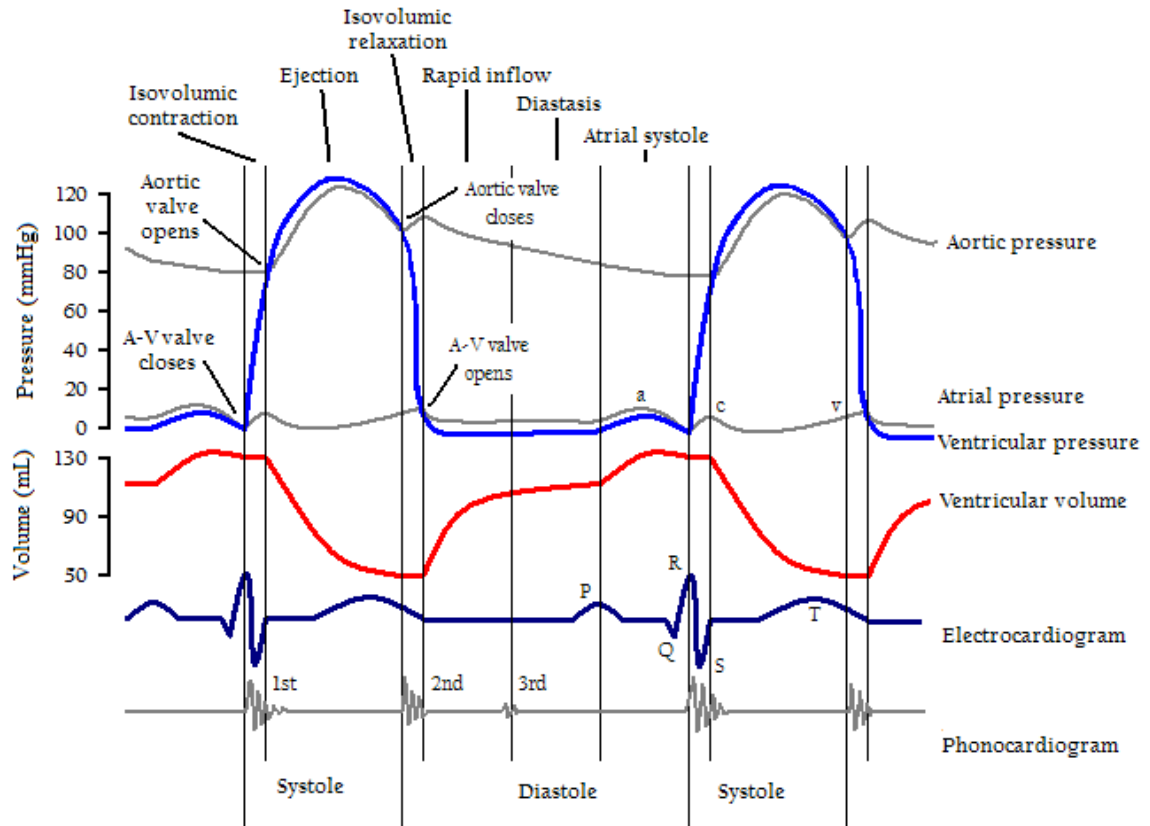


**Figure 1.4: Wiggers Diagram of a cardiac cycle**

([en.wikipedia.org/wiki/File:Wiggers\\_Diagram.png](https://en.wikipedia.org/wiki/File:Wiggers_Diagram.png))

**Table 1.1: Phases and stages of cardiac cycle**

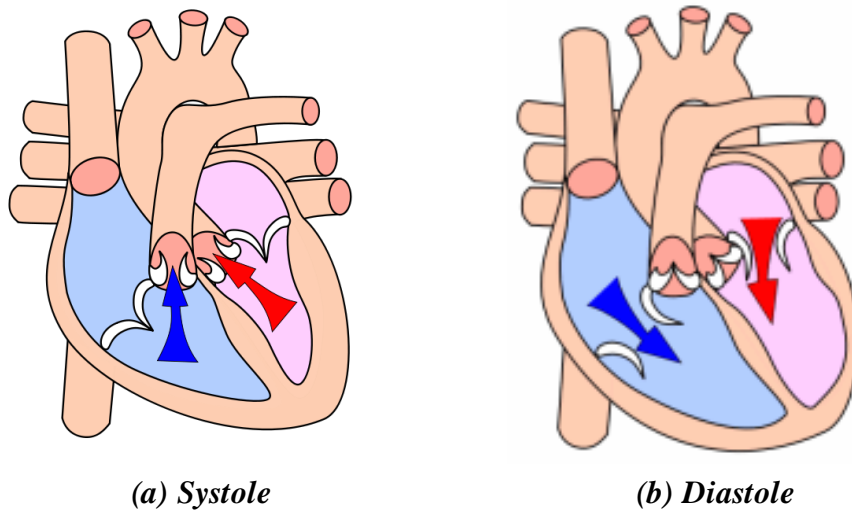
Cardiac phases	Cardiac stages	Av valves	Semilunar valves
Systole	1. Isovolumetric contraction	Closed	Closed
	2. Ventricular ejection	Closed	Open
Diastole	3. Isovolumetric relaxation	Closed	Closed
	4. Ventricular filling and atrial diastole	Open	Closed
	5. Ventricular filling and atrial systole	Open	Closed

Ventricular systole starts from the QRS complex which can be detected by electrocardiography (ECG) (shown in Figure 1.4). During systole (shown in Figure 1.5a),



blood is pumped out of the heart from the left ventricle to systemic part of the body via the aortic valve, and from the right ventricle to the lungs via the pulmonic valve. The first two cardiac stages are at systole. In the first stage, since ventricles commence contraction but both valves are closed (shown in Table 1.1), no blood can go in or out of the ventricle. Thus, the ventricle is undertaking an isovolumetric contraction with a dramatically rising pressure (from time A to time B on Figure 1.6). In the second stage (from time B to time C on Figure 1.6), ventricles continue to contract with a decreasing ejection rate. Eventually they reach minimum volume, which is known as end systole (ES).

During diastole (shown in Figure 1.5b), blood is coming back to the heart because of relaxation. The oxygenated blood travels from the left atrium via the mitral valve to fill the left ventricle, while the deoxygenated blood travels from the right atrium via the tricuspid valve to fill the right ventricle. The next three cardiac stages commence at diastole. In the third stage, since both valves are closed again due to ventricular relaxation, volume stays the same. When ventricles continue to relax, pressure drops rapidly (from time C to time D on Figure 1.6). The fourth stage is known as early diastole, when both the atria and ventricles are relaxed and passively filled in decreasing rate. In the fifth stage, an atrial systole, the P wave appeared in ECG curve (Figure 1.4), indicates the beginning of late diastole. As atria contract, blood is driven into ventricles again. The additional flow of blood is known as the atrial kick. Ventricles reach maximum volume at the end, which is known as end diastole (ED).



([en.wikipedia.org/wiki/File:Heart\\_systole.svg](http://en.wikipedia.org/wiki/File:Heart_systole.svg)) ([en.wikipedia.org/wiki/File:Heart\\_diastole.png](http://en.wikipedia.org/wiki/File:Heart_diastole.png))

*Figure 1.5: Schematic of blood circulation with red arrows as oxygenated blood and blue arrows as deoxygenated blood*

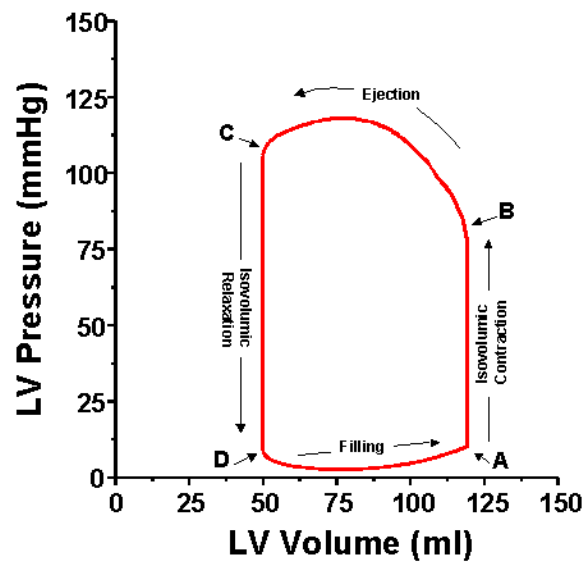


*Figure 1.6: Pressure volume loop of a typical human cardiac cycle (Center for Teaching and Learning in Columbia, 2016)*

## 1.4 Segmentation of the Heart

Depicted in Figure 1.7, in order to generate tomographic images, three cardiac planes are introduced during MRI (American Heart Association et al., 1992). These three corresponding views are perpendicular to each other. Two chambers, left ventricle and atrium, are seen in the vertical long-axis (VLA) view, while all four chambers are shown in the horizontal long-axis (HLA) view.

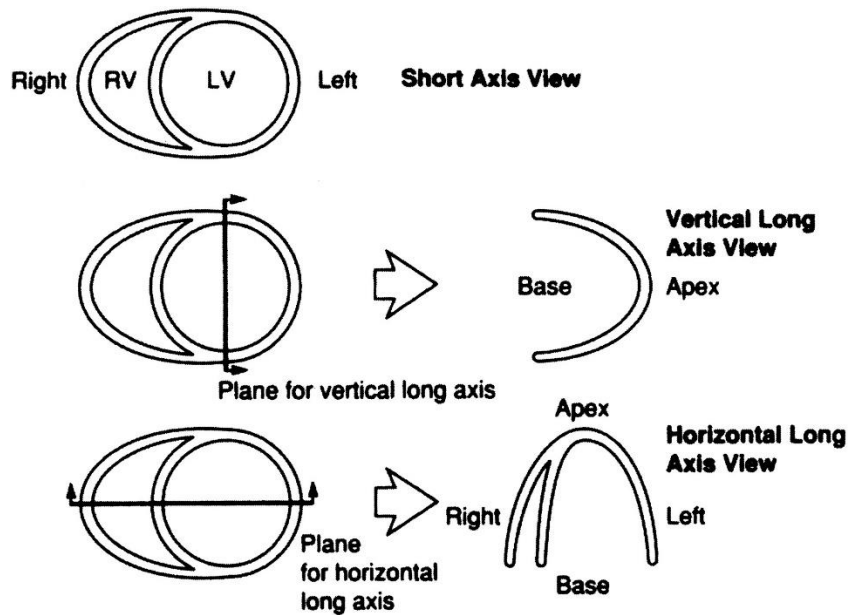


**Figure 1.7: Definitions of short axis (SA), vertical long-axis (VLA), and horizontal long-axis (HLA) views (Cerqueira, 2002)**

For regional analysis of ventricular function and myocardial perfusion, segmentation of the heart is necessary. Typically, 9 segments are employed for clinical applications in CMR (Cerqueira, 2002). A 9-segment model includes 1 apical segment (Figure 1.8b and

Figure 1.8c), 4 mid-ventricular segments (Figure 1.8a), and 4 basal segments (Figure 1.8a) (Slart et al., 2004).

Along the direction of ventricular long axis, the LV is divided into equal thirds (apical, mid-ventricular, and basal slices) at end diastole. If the actual number of short-axis slices is more than three, all short-axis slices are then summed to create three thick short-axis slices. The true apex lies beyond the end of the left ventricular cavity. It can be evaluated from the 4-chamber view and 2-chamber view.

As shown in Figure 1.8a, a myocardial ring corresponds to a short-axis section through the LV. Instead of right and left, the sides of each ring are named as septal and lateral. Likewise, the top and bottom of each ring are named as anterior and inferior respectively. From a view of human body, the septal side is closer to the chest than the lateral side. With regard to the circumferential location, two insertion points of the RV wall to the LV separate myocardium into septum and free wall, and the free wall has three evenly-distributed segments.

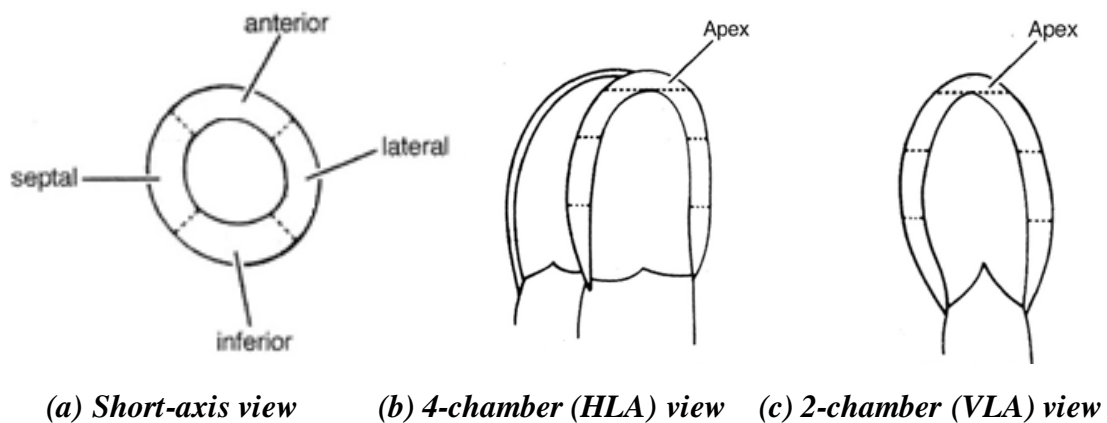


**Figure 1.8: Schematic of segmentation of left ventricle (Cerqueira, 2002)**

As American Heart Association (AHA) suggested (Cerqueira, 2002), each segment can be assigned to one of the 3 major coronary arteries of the left anterior descending (LAD), right coronary artery (RCA), and the left circumflex coronary artery (LCX). Their locations are demonstrated in Figure 1.9 and Figure 1.10.

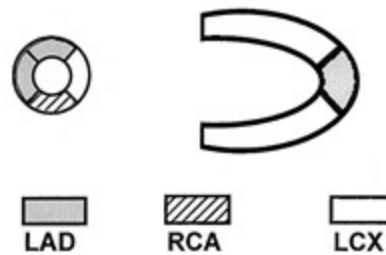


**Figure 1.9: Assignment of the myocardial segments to specific coronary artery territories (Cerqueira, 2002)**

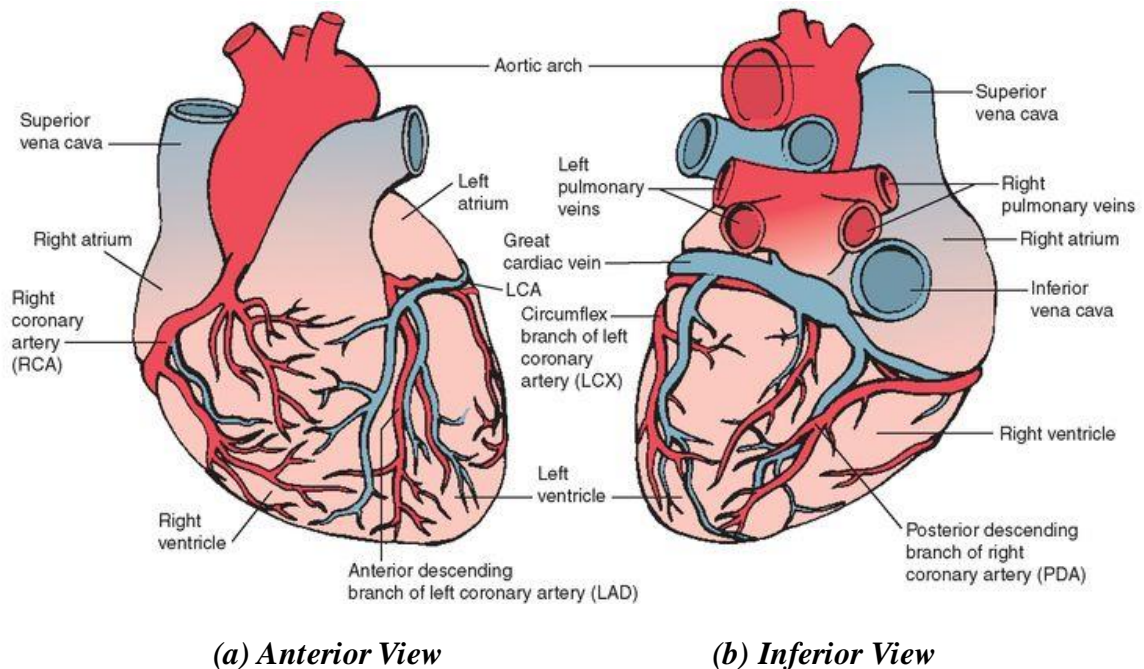


**Figure 1.10: Coronary arteries and major veins of the heart (Sky, 2017)**

## 1.5 Cine Displacement ENcoding with Stimulated Echoes (DENSE) MRI

Cine Magnetic Resonance Images are basically short movies with the ability to display average heart motion throughout the cardiac cycle. And DENSE technique provides tissue tracking which allows the analysis of myocardial deformation. As a result, a detailed profile of regional cardiac mechanics can be generated non-invasively.

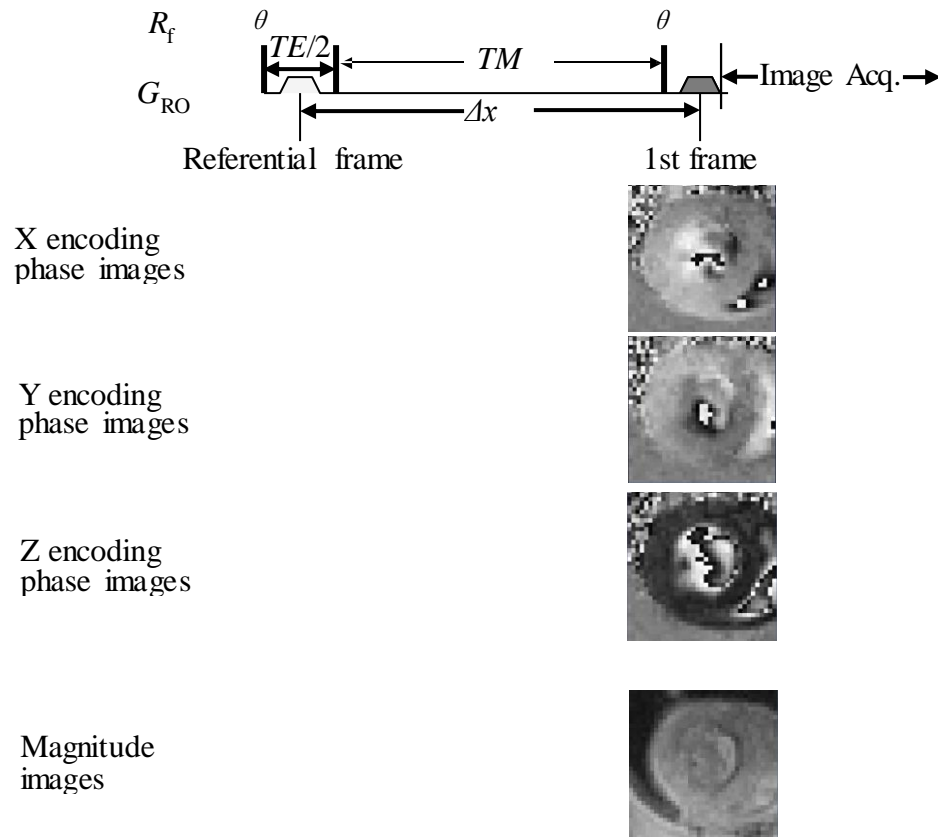


**Figure 1.11: DENSE pulse sequence and representative outputs of DENSE acquisition**

A diagram of DENSE acquisition protocol is depicted in Figure 1.11 and a spiral pulse sequence for one frame sampling is demonstrated in Figure 1.12. Once the R wave in the

electrocardiogram is detected, the sequence is triggered and an initial  $R_f$  excitation with a specific flip angle  $\theta$  is emitted. Meanwhile, imaging with slice selection is performed by applying a magnetic gradient  $G_{ss}$ . Subsequently, two magnetic readout gradients  $G_{FE}$  and  $G_{PE}$  are generated in two orthogonal directions of a plane.  $G_{FE}$  and  $G_{PE}$  are  $k$ -cycle sinusoidal waves oscillating with a slowly increasing amplitude until they reach the amplitude limit. If a single effective readout gradient  $G_{RO}$  is assumed to be the vector sum of  $G_{FE}$  and  $G_{PE}$ ,  $G_{RO}$  rotates with the fluctuations in  $G_{FE}$  and  $G_{PE}$  and spirals out with the increasing amplitudes of  $G_{FE}$  and  $G_{PE}$ . Consequently,  $G_{RO}$  marches on the plane via a  $k$ -space trajectory. Figure 1.13a shows a single  $k$ -space trajectory proceeded in a single readout window. This is referred to as an Archimedean spiral which can be expressed as an angle  $\theta$  in terms of the radius of a specific trajectory point. By comparison, Figure 1.13b shows four interleaved  $k$ -space trajectories carried out in four readout windows. For the same spatial resolution, an interleaved spiral scan can bring more signal than a single-shot spiral scan did, which leads to less blurring at the cost of longer scan time. As  $G_{RO}$  spirals out, phase dispersion is introduced in a direction perpendicular to  $G_{RO}$  across tissue. Since  $G_{RO}$  proceed in a  $k$ -space trajectory, phase dispersion also proceeds on the plane via a  $k$ -space trajectory. As a result, echo of radiation caused by a magnetic moment change is recorded along those trajectories from the center to the periphery again and again until a circular field of view (FOV) is fully covered. Here,  $G_{RO}$  is assumed to have a magnitude

$G_R$  G/cm and a duration time  $t_{enc}$  (period of a readout window). The sampling for the referential frame is done.

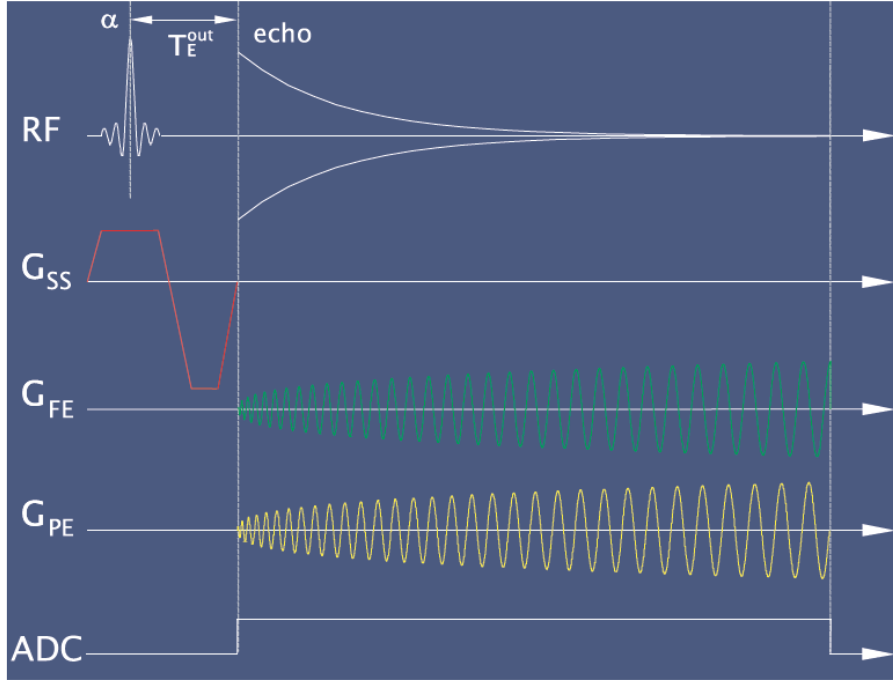


**Figure 1.12: Timing diagram for the 3D cine DENSE spiral pulse sequence (Faro and Mohamed, 2006)**

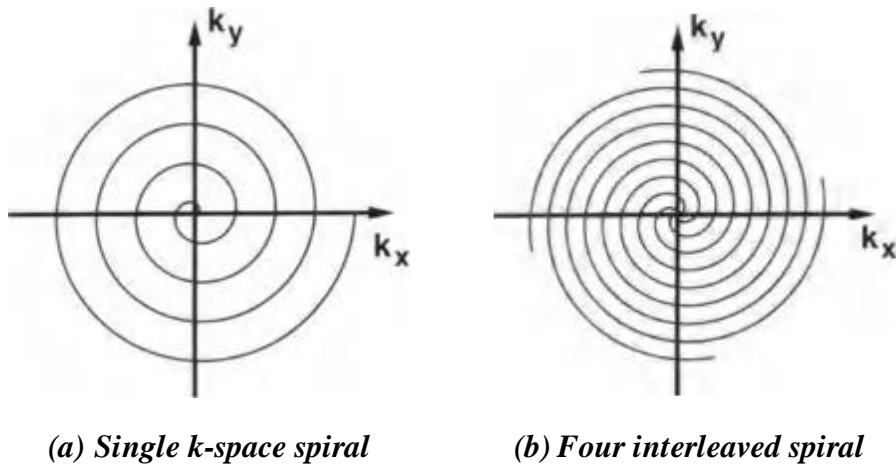


**Figure 1.13: Diagram of  $k$ -space trajectories covered over a field-of-view (Meyer, 1998)**



The sampling for the first frame is conducted using the same sequence for the referential frame. Specifically, when the second  $R_f$  excitation is applied, tissues have moved a distance of  $\Delta x$  during a time period of  $TR$ , followed by a second effective readout gradient  $G_{RO}$  causing another phase dispersion. For stationary spins, the phase dispersion is completed. For protonic spins which have a displacement of  $\Delta x$ , a net phase  $\varphi_1$  of the echo signal is accumulated, which is illustrated by Equation (1.1):

$$\varphi_1 = \gamma_H G_R t_{enc} \Delta x \quad (1.1)$$

where  $\gamma_H$  is the gyromagnetic ratio in Hz/Tesla.

Later on, the sampling for each frame is performed per  $R_f$  excitation with  $TR$  as repetition time. Thus, a scan is an  $n$ -frame sampling at a cardiac cycle. During one scan, a cardiac cycle is split into multiple frames depending on the heart rate. The heart throughout the cardiac cycle is repeatedly imaged with the same slice selection.

Phase encoding of displacements is conducted by repeating scans. In order to obtain displacements in the FOV throughout the cardiac cycle, the first scan serves as the phase reference data set. After this, a complementary data set is acquired by repeating the procedures of the first scan once more with altered amplitude  $G_R'$  as the effective readout gradient  $G_{RO}$ . In order to encode displacement effectively, the difference in effective readout gradients is set for a specific value. Take the first-frame sampling as example, since the amplitude of effective readout gradient changes to  $G_R'$ , accumulated phase  $\varphi_2$  is different (illustrated by Equation (1.2)). Thus, the phase shift  $\Delta\varphi$  between two sequences

can be used to compute  $\Delta x$  (illustrated by Equation (1.3)). Although the difference of effective readout gradient is small, a large displacement of  $\Delta x$  can occur when  $TR$  is set to be large enough so that a noticeable phase difference  $\Delta\phi$  can be detected. That's why DENSE can have a high spatial resolution (Aletras et al., 1999).

$$\phi_2 = \gamma_H G_R' t_{\text{enc}} \Delta x \quad (1.2)$$

$$\Delta\phi = \gamma_H (G_R - G_R') t_{\text{enc}} \Delta x \quad (1.3)$$

In order to acquire displacements in three directions, a balanced four-point encoding strategy was developed by Zhong and colleagues (Zhong et al., 2009). It can suppress homogeneous phase noise in three directions and increase phase signal-to-noise ratio (SNR) (Zhong et al., 2009). Specifically, a phase reference scan and a complementary scan are performed on the four vertices of a regular tetrahedron, respectively (shown in Figure 1.14). In order to get the 3D displacements in the centroid of the tetrahedron, four sets of phase differences corresponding to four vertices are acquired. Next, x, y, and z displacements are derived from phase differences using weighting vectors. Last, tissue displacement values are encoded directly into the intensity of each pixel of phase images along each direction. Overall, a total of eight cine MRI scans are conducted for encoding phase images along three directions, presenting a map of 3D displacement of tissue of interest on a specific slice.

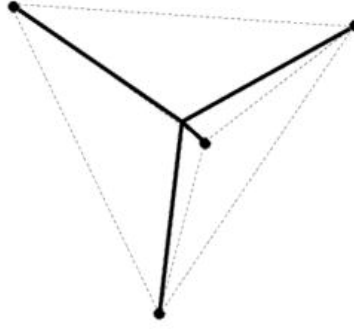


***Figure 1.14: Four weighting vectors for 3D balanced multi-point encoding method***

***(Zhong et al., 2009)***

Magnitude images are averaged over the phase reference scans so that each image is the information obtained during the same frame across multiple cardiac cycles. In order to generate tomographic images depicted in Figure 1.7, three cardiac planes are introduced during MRI (American Heart Association et al., 1992). These three corresponding views are perpendicular to each other. Two chambers, left ventricle and atrium, are seen in the vertical long-axis (VLA) view, while all four chambers are shown in the horizontal long-axis (HLA) view.

In order to fully assess the entire heart, separate cine image sets are acquired at various locations, like base, middle ventricle, and apex for short-axis images, or in various views, like 2-, 3-, and 4-chamber views for long-axis images. At last, the series of magnitude images are gathered together to produce a movie (cine).

Figure 1.11 shows a  $T_1$  weighted magnitude image. The black blood is caused by the nonsynchronous motion of the blood in the ventricle. This type of image contrast is desirable in our cardiac MRI studies. First, black blood gives a high contrast between

myocardium and ventricular cavity, which helps us to distinguish them. Second, the motion of bright blood can produce artifacts along the phase direction (shown in Figure 1.15).

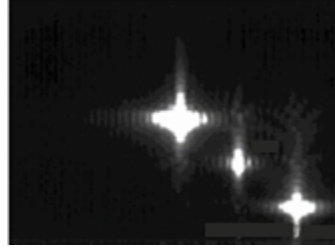
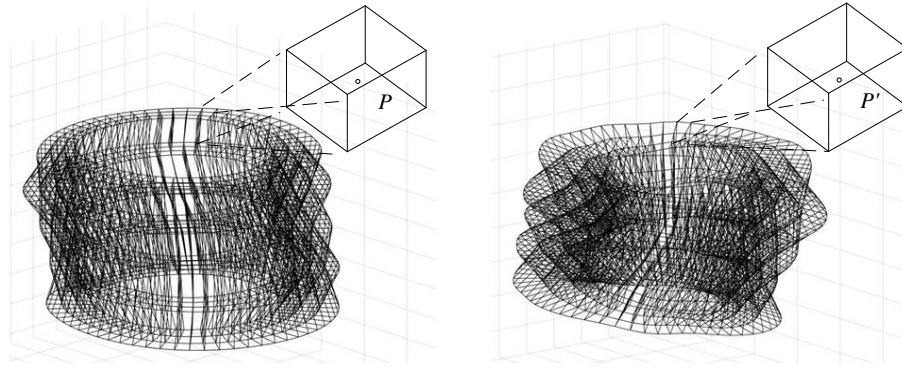


**Figure 1.15: Striping Artifacts caused by bright blood signal (Aletras et al., 1999)**

## 1.6 Computing Mechanics

By definition, the referential mesh is the referential configuration of the heart in the referential frame, while the computational mesh is the current configuration of the heart in a specific frame (time  $t$ ).



**(a) A referential mesh**

**(b) A computational end-systolic mesh**

**Figure 1.16: Left ventricular volumetric meshes.**  $60 \times 3 \times 4$  elements were built in circumferential, transmural and longitudinal directions reconstructed from the MRI images scanned on Aug. 30, 2015. An 8-noded brick element is in an arbitrary location of the mesh

Considering an 8-noded brick element in an arbitrary location of the mesh (shown in Figure 1.16), it's denoted as  $P$  located at  $\underline{X}$  in the referential mesh and  $P'$  located at  $\underline{x}$  in the computational mesh, where  $\underline{X}$  and  $\underline{x}$  are both defined in a 3D Cartesian coordinate system. Its deformation can be calculated using coordinates of eight vertices and the centroid. The current deformation  $d\underline{x}$  of  $P'$  can be mapped into the referential deformation  $d\underline{X}$  of  $P$ . Thus, the deformation gradient tensor  $\underline{F}$  can be defined by:

$$\underline{F} = \frac{\partial \underline{x}(\underline{X}, t)}{\partial \underline{X}} \quad (1.4)$$

The Jacobian deformation  $J$  is calculated by:

$$J = \det \underline{F} \quad (1.5)$$

The Lagrangian strain tensor in Cartesian coordinates is equal to:

$$\underline{E} = \frac{1}{2} (\underline{F}^T \underline{F} - \underline{I}) \quad (1.6)$$

where  $\underline{I}$  is the identity tensor. Six independent components of  $\underline{E}$  are corresponding to three normal strains and three shear strains in Cartesian coordinates.

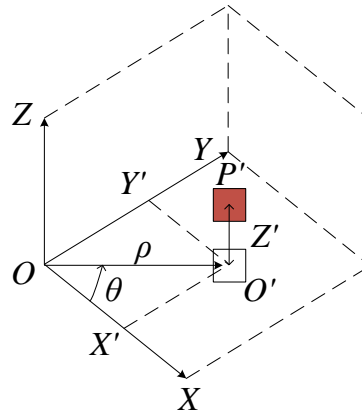


**Figure 1.17: Transformation from Cartesian coordinates to polar coordinates**

To simplify, all elements slightly above or below the slice of interest are considered to be located on the same plane., and these elements are assumed to be distributed circularly. Depicted in Figure 1.17, point  $O$  is the center of the distribution circle where the element  $P'$  is closest to. The centroid of the element is mapped to point  $O'$ , where  $X'$ ,  $Y'$  and  $Z'$  are Cartesian coordinates of the centroid. Thus, the angle  $\theta$  is defined by:

$$\theta = \tan^{-1} \frac{Y'}{X'} \quad (1.7)$$

The rotation matrix  $R$  is defined by:

$$R = \begin{bmatrix} \cos \theta & \sin \theta & 0 \\ -\sin \theta & \cos \theta & 0 \\ 0 & 0 & 1 \end{bmatrix} \quad (1.8)$$

and can transform the Cartesian coordinate system into the polar coordinate system. Hence, the Lagrangian strain tensor in polar coordinates can be derived by:

$$\underline{E}_{\text{polar}} = R \underline{E} R^T = \begin{bmatrix} E_{rr} & E_{rc} & E_{rl} \\ E_{cr} & E_{cc} & E_{cl} \\ E_{lr} & E_{lc} & E_{ll} \end{bmatrix} \quad (1.9)$$

where  $E_{rr}$  is radial strain,  $E_{cc}$  is circumferential strain,  $E_{ll}$  is longitudinal strain,  $E_{rc}$ ,  $E_{rl}$  and  $E_{cl}$  are shear strains relative to two corresponding directions, respectively.

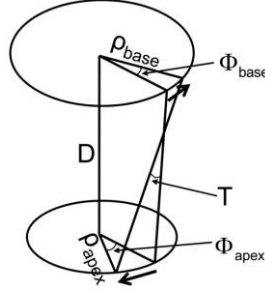


**Figure 1.18: Definition of torsion  $T$  between basal and apical slices (Rüssel et al., 2009)**

The circumferential-longitudinal (CL) shear angle  $\alpha_{CL}$  is used to describe torsion because it's normalized with respect to the radius  $\rho$  of a myocardial slice and the distance  $D$  between slices (Figure 1.18). The value of  $\alpha_{CL}$  can be obtained by Equation (1.10) (Rüssel et al., 2009).

$$\alpha_{CL} = \sin^{-1} \frac{2E_{cl}}{\sqrt{(1+2E_{cc})(1+2E_{ll})}} \quad (1.10)$$

The positive value of  $\alpha_{CL}$  indicates a counterclockwise rotation as observed from the apex to base.

## **2 Quantification of 3D Lagrangian Strain and Torsion in Rat Left Ventricles under Inotropic Stimulation using 3D cine DENSE MRI**

### **2.1 Background**

Literatures suggest that heart disease might cause a statistically significant change in cardiac mechanics, such as strains and torsion, which can provide diagnostic information for deciding medical therapies (Chen et al., 2010; Haggerty et al., 2013a; Hess et al., 2009; Li and Yu, 2010; Liu et al., 2004; Zhong and Yu, 2010a).

Rat models have been increasingly used in the research of cardiac diseases, including myocardial infarction (Goldman and Raya, 1995), pulmonary hypertension (Fomovsky et al., 2009), and age associated heart failure (Patten and Hall-Porter, 2009). The application of a 12-segment ventricular model can provide a more detailed profile of regional cardiac mechanics, which is related to the 3 major coronary arteries. The regional difference of Lagrangian strains can serve as useful reference for evidence-based medical therapies.

Since isoproterenol is an inotrope, it will cause increased contractility in the heart. Specifically, the heart beats harder with acute administration under isoproterenol stimulation. The hypothesis is that cardiac mechanics in rat LV under isoproterenol stimulation will exhibit regional differences. The change in myocardial strain in rat hearts caused by isoproterenol stimulation can provide the reference for understanding how inotropic drugs, which are used in stress tests, cause changes in regional contractility. This

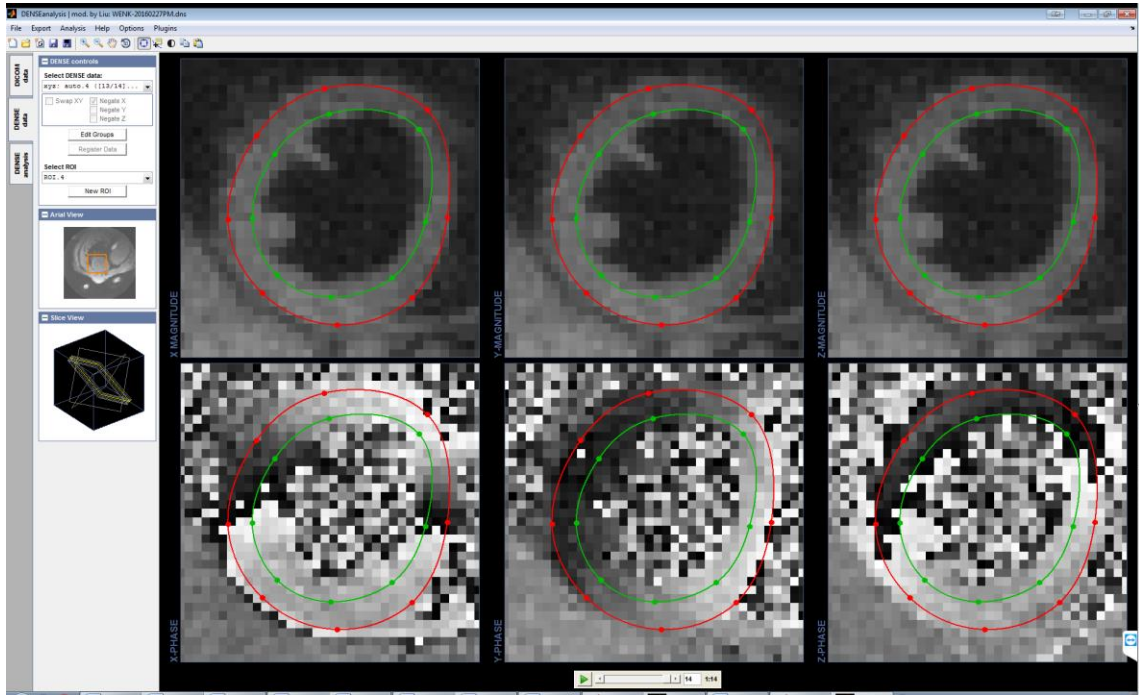


reference could then be compared to a diseased model, under inotropic stimulation, to identify regional disruptions in function and potentially help in the determining treatment.

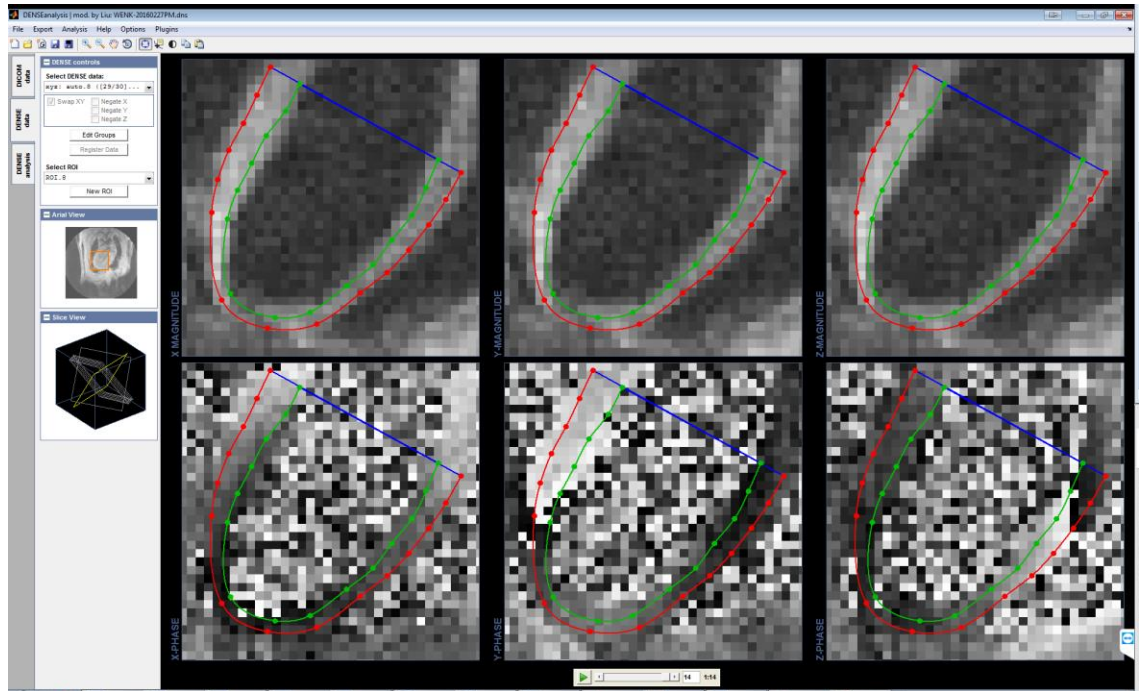
## **2.2 Methods**

### **2.2.1 Myocardial Segmentation**

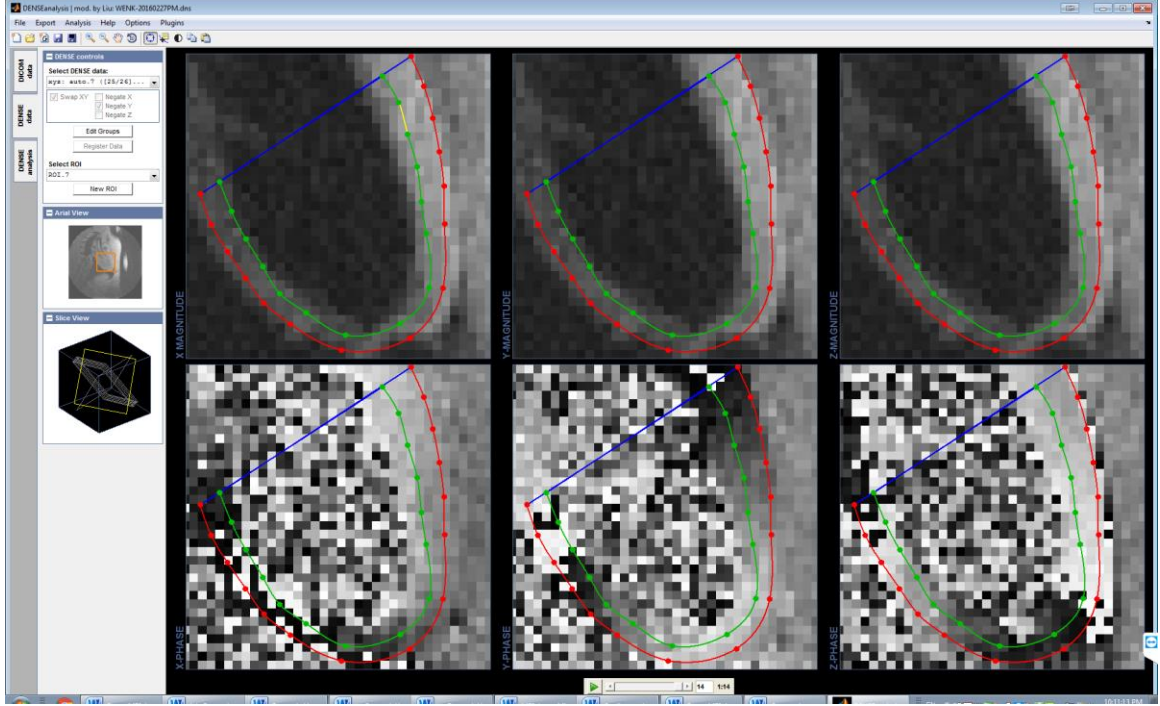
It should be noted that DENSE MRI acquisition was conducted by Dr. Xiaoyan Zhang, a former postdoctoral scholar in the lab. In this study, 10 healthy and 9 isoproterenol-simulated female Sprague-Dawley rats (approximately 6 months of age) were scanned using a 7-Tesla BrukerClinScan system (Bruker, Ettlingen, Germany). An open-source application DENSEanalysis (Gilliam et al., 2016; Spottiswoode et al., 2007) developed in MATLAB was used as the image segmentation tool. The contours of endocardium and epicardium of left ventricle were drawn on both short-axis and long-axis images (Figure 2.1). Blood pool and surrounding tissue were identified by the dark regions in magnitude images and noisy pixels in phase images. Endocardial and epicardial boundaries were traced in all frames and slices to verify that the myocardium has a smooth deformation.



(a) *Short-axis contours viewed from the apex*



(b) *Vertical long-axis contours*



(c) *Horizontal long-axis contours*

**Figure 2.1: Left ventricular contours at isoproterenol-simulated end diastole of mid-ventricle.** Images were taken on Feb. 27, 2016. Red curves are epicardial contours. Green curves are LV endocardial contours. Yellow curves are RV endocardial contours.

Subsequently, myocardial contours need to be modified by excluding the papillary muscles. Because papillary muscles (2 protrusions in Figure 2.2) were aligned from the left middle ventricle up to the base (Figure 2.3b), a segment of endocardial contours may be wrongly placed on them when the contours were drawn on short-axis images. If papillary muscles are inside myocardial contours, they could increase wall thickness tremendously from one slice to another slice (Figure 2.3a). Besides, since papillary muscles are pulling

atrioventricular valves during diastole, they would be invisible and hard to be tracked, especially at ED. In other words, the papillary muscles inside myocardial contours can lead to a large fluctuations in wall deformation longitudinally and temporally. Thus, papillary muscles need to be excluded from myocardial contours.

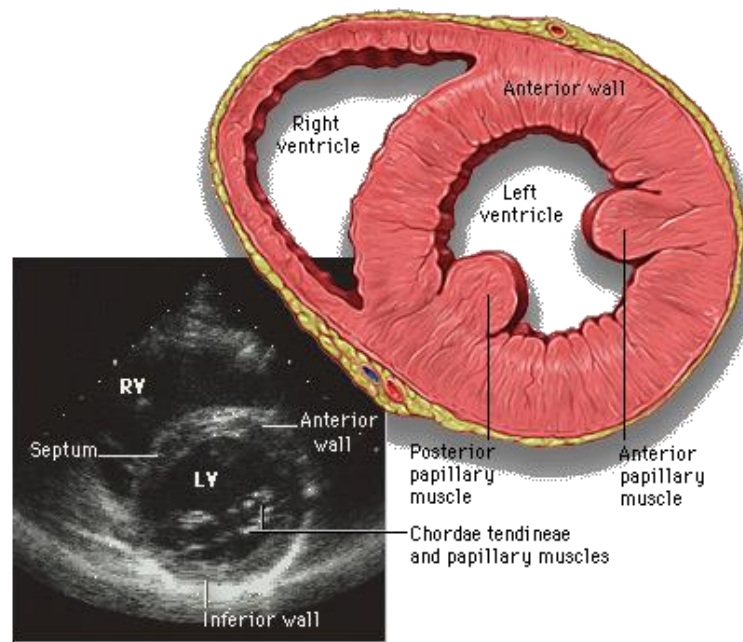
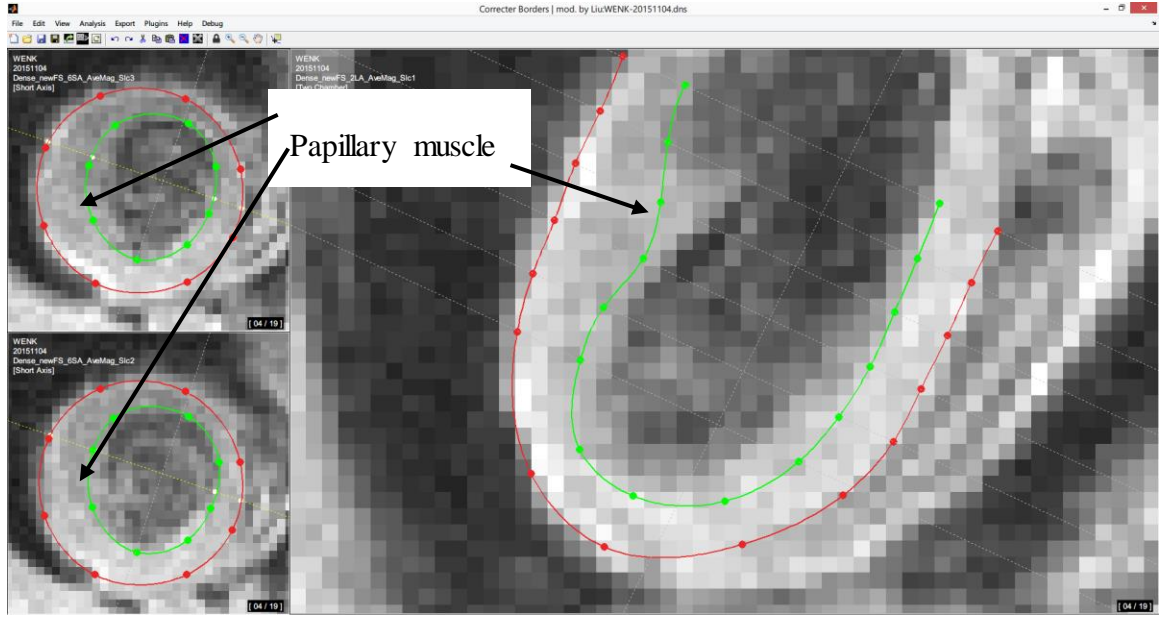


**Figure 2.2: Papillary muscles in human heart ([criticalecho.com](http://criticalecho.com))**

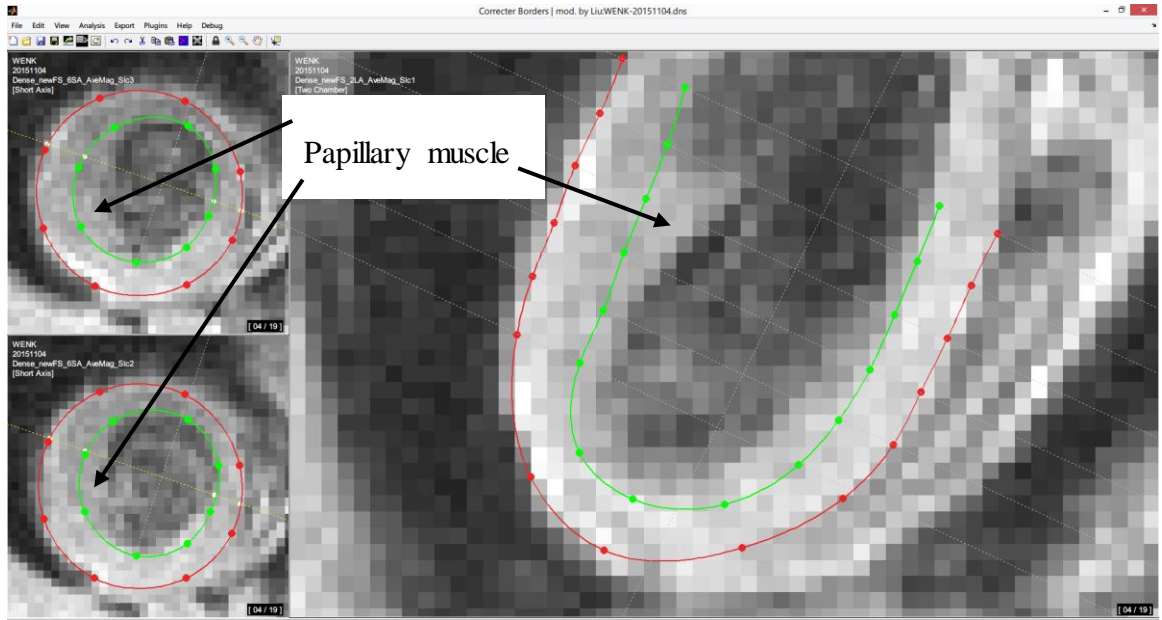
Fortunately, papillary muscles in rat heart were large enough to be visualized at end systole from long-axis view. Thus, short-axis contours need to be displayed on long-axis images to verify they don't cover papillary muscles. An application called CorrecterBorders, which was developed by Dr. Jonathan Suever, can display 3D freehand contours simultaneously on both short-axis and long-axis CMR images of DICOM standard. In order

to make the contours created by DENSEanalysis be compatible with the contours created by CorrecterBorders, two custom modules were written in MATLAB (Mathworks, Inc., Natick, MA). Specifically, through associating short-axis images with long-axis images based on locations and orientations of all slices, 2D contours created with DENSEanalysis were converted to 3D contours read by CorrecterBorders. As shown in Figure 2.3a, papillary muscle was hard to be identified in a short-axis view but well-marked from a long-axis view. After modifications of short-axis contours (Figure 3.7b) with CorrecterBorders, the contours were imported back to DENSEanalysis for further adjustments.





*(a) Before adjustment*



*(b) After adjustment*

**Figure 2.3: Exclusion of papillary muscle from myocardial contours**

Furthermore, the methodology of excluding papillary muscle is also applied to the adjustment of apical contours, since magnitude images are noisy in the apical slice where myocardium is more difficult to be segmented from the blood pool. Subsequently, apical

contours were adjusted by assuming consistent wall thickness in SA and LA views, respectively.

Last but not least, a fine tuning was conducted on myocardial contours based on the following principles of ventricular shapes changing in a particular cardiac stage. First, myocardial contours are supposed to have same size during isovolumetric contraction or isovolumetric relaxation. Second, myocardial contours are supposed to shrink with increasing wall thickness during systole, but enlarge with decreasing wall thickness during diastole.

### **2.2.2 Discretization of the LV in the Referential Frame**

Once myocardial contours were done, a module (Spottiswoode et al., 2007) in DENSEanalysis was used to generate the cardiac model slice by slice. For the slice of interest, a cardiac model consists of resting contours in the referential frame and  $n$  computational contours in each imaging frame. As shown in Figure 2.4, resting contours are displayed in the left viewer, while the computational contours of frame 20 are in the right viewer.

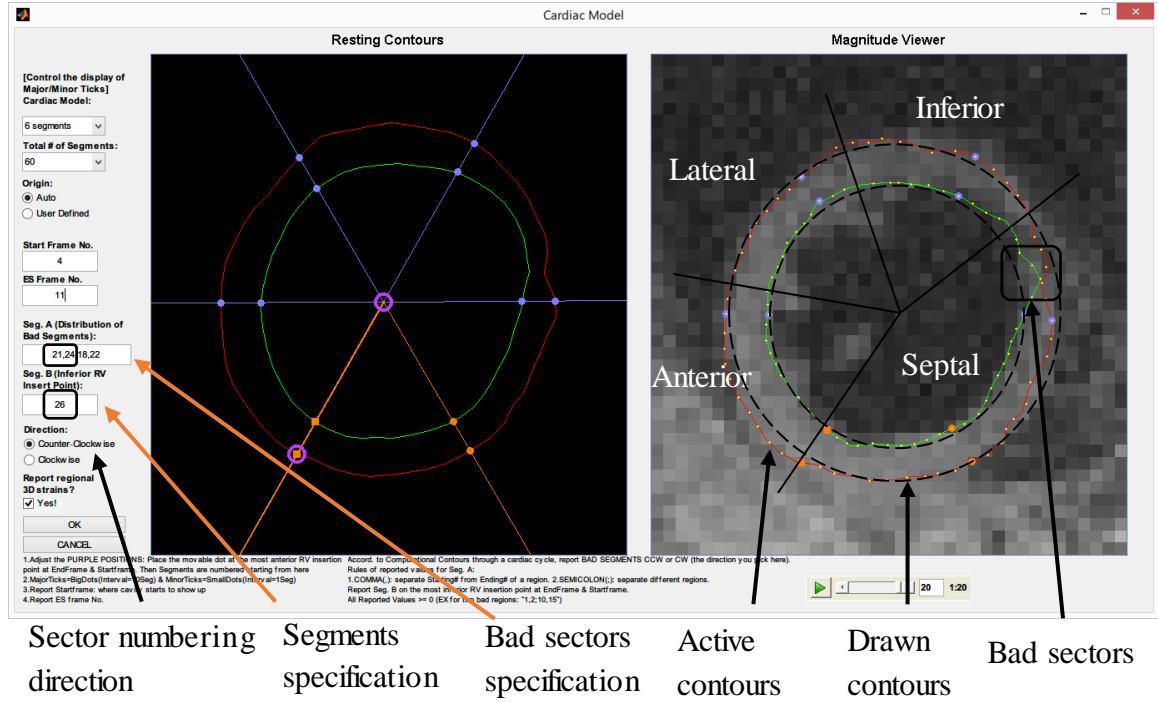


**Figure 2.4: Meshing user interface for a short-axis slice**

As shown in Figure 2.4, a custom mesh configuration interface was created with graphical user interface design environment (GUIDE) of MATLAB. Additionally, a corresponding mesh configuration module was also developed and integrated into the self-developed application called 3D DENSE Plugin for Crescent Organ (Liu, 2018). The mesh configuration module is capable of the following three functions.

First, the 12-segment model is applied to the cardiac model. As shown in Figure 2.4, myocardium was separated into septum and free wall by defining two insertion points of the RV wall to the LV wall. The anterior RV insertion point was set by the placement of the square dot, while the inferior RV insertion point was defined by reporting the sector number



on it. And free wall was divided into equal thirds which were classified as inferior, lateral, and anterior segment, respectively.

Second, user-defined meshing of the left ventricle was based on a finite element mesh interpolation scheme. As shown in Figure 2.4, all computational contours in the slice were set for a circumferential partition of 60 sectors numbered counterclockwise. Four nearby yellow dots constructed a sector. By default, the first sector was placed on the anterior RV insertion point (the square dot in Figure 2.4). Each sector is attributed to its corresponding segment based on its circumferential location.

Last but not least, noise of DENSE images was suppressed by marking bad sectors. Bad sectors were caused by wrong selection of unwrapped pixels or noise of DENSE magnitude and phase images. If bad sectors still exist after trying different unwrapped pixels from different frames, it is necessary to remove the bad sectors. For example, compared with the drawn contours at end diastole (two black dash circles in Figure 2.4), computational contours (two green solid curves in Figure 2.4) have abnormal wall thickness from sector 21 to sector 24, resulting in enormous magnitude of the strain components. Reporting the numbers of bad sectors made them inaccessible to the application, i.e., they were not used in assessing the deformation. It should be noted that the bad sectors were typically found at the RV insertion points.

As a result, the referential mesh and computational meshes were created in 3D DENSE Plugin for Crescent Organ (Liu, 2018) (shown in Figure 1.16). Since coordinates of eight

vertices of each element were known, the Lagrangian strain tensor was calculated in each element, which is discussed in the Section 1.6. Strain of each segment was evaluated by averaging the strains of good elements inside it, which was implemented by a custom script written in MATLAB.

### 2.2.3 Segmentation of the LV Mid-ventricle

Considering that there is a variation in heart sizes between animals, the middle ventricle is assumed to locate at the half length of the left ventricular cavity based on the long-axis endocardial contours at end systole.

A 12-segment model is applied to the LV middle ventricle (shown in Figure 2.5) and segment names are summarized in Table 2.1. Specifically, the middle ventricle was divided into septal, lateral, inferior and anterior segments circumferentially and transmural thirds (sub-endocardium, mid-wall, and sub-epicardium). By definition, the anterior segment lies by the side which is closer to the chest.

***Table 2.1: Notation of LV mid-ventricular segments***

Septal segments	Inferior segments	Lateral segments	Anterior segments
1. Septal sub-endocardium	2. Inferior sub-endocardium	3. Lateral sub-endocardium	4. Anterior sub-endocardium
5. Septal mid-wall	6. Inferior mid-wall	7. Lateral mid-wall	8. Anterior mid-wall
9. Septal sub-epicardium	10. Inferior sub-epicardium	11. Lateral sub-epicardium	12. Anterior sub-epicardium

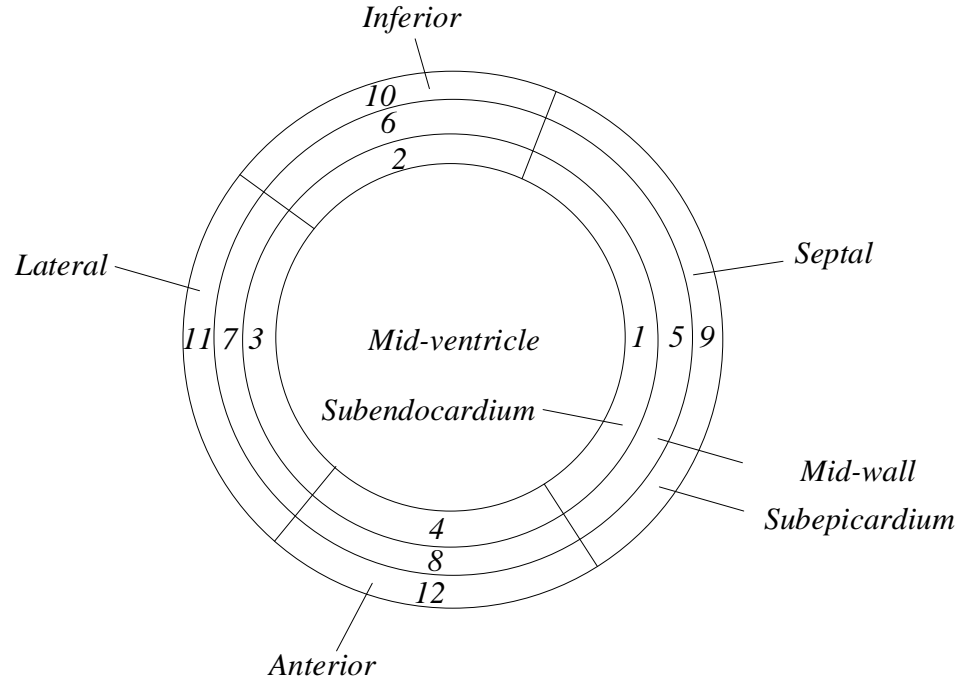


**Figure 2.5: A 12-segment model at mid ventricle**

#### **2.2.4 Statistical Analysis**

Data were represented as mean  $\pm$  standard error of the mean (SEM). Single comparisons for the differences in hemodynamic parameters between control and isoproterenol-treated rats were conducted with unpaired student t-test. Multiple comparisons related with strain components or CL shear angle in each transmural layer were conducted using 2-way ANOVA with post-hoc Bonferroni t-tests. A value of  $p < 0.05$  was considered significant.

### **2.3 Results**

#### **2.3.1 Global Function of LV**

Changes in cardiac function are summarized in the Table 2.2. Specifically, significant increase in heart rate (HR) and ejection fraction (EF) was detected under isoproterenol

stimulation. And maximum rates of LV pressure rise and fall were increased significantly in isoproterenol-infused rats, which indicate that LV contraction and relaxation were enhanced statistically.

**Table 2.2: Hemodynamic parameters in baseline and isoproterenol-infused rats.**

*\*p < 0.05. (Zhang et al., 2018)*

	Baseline	Isoproterenol-infused rats
Heart rate (bpm)	334 ± 7	432 ± 8*
LV end-diastolic pressure (mmhg)	12.5 ± 0.9	13.3 ± 0.9
Peak LV systolic pressure (mmhg)	115.1 ± 2.5	121.8 ± 2.7*
Maximum rates of LV pressure rise (mmhg/s)	9213 ± 399	13553 ± 858*
Maximum rates of LV pressure fall (mmhg/s)	10867 ± 325	15354 ± 1631*
LV end-diastolic volume (μl)	311 ± 11	291 ± 13
LV end-systolic volume (μl)	130 ± 6	87 ± 6*
LV stroke volume (μl)	181 ± 11	204 ± 9
LV ejection fraction (%)	58 ± 2	70 ± 1*

A custom script was written in MATLAB for comparing strains in rat left ventricles at baseline and under isoproterenol stimulation. Since the subjects have different heart rates, strain in terms of temporal frames were transferred into strain in terms of percentage of the cardiac cycle. A temporal interpolation was done by fitting a cubic spline into scattered strain values distributed over time.

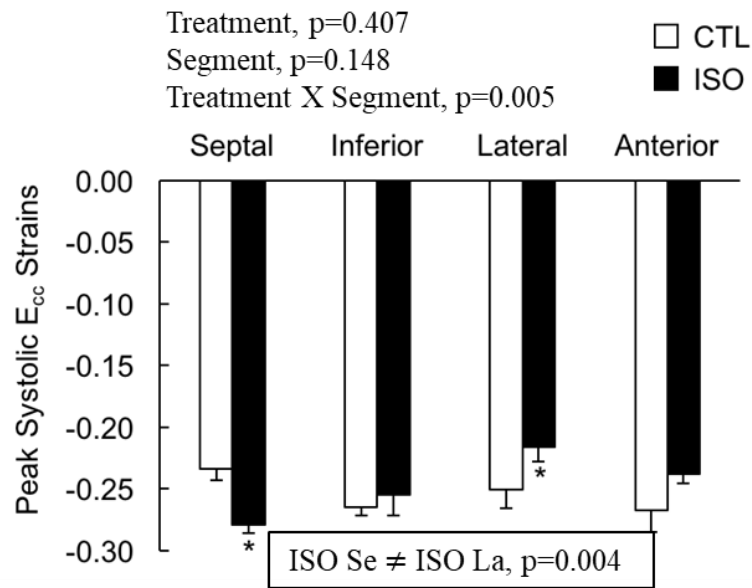
First of all, the global effect of isoproterenol on the peak Lagrangian strains and torsion of in the LV was investigated and the results are summarized in the Table 2.3. Specifically, significant increases in  $E_{rr}$ ,  $E_{cl}$  and CL shear angle are found at either basal, mid-ventricular, or apical regions of the LV, indicating isoproterenol has a more significant impact on the radial wall thickening and ventricular torsion compared with circumferential shortening or longitudinal shortening in terms of mechanical deformations of myocardium.

**Table 2.3: Effects of isoproterenol on the global peak Lagrangian strains and circumferential-longitudinal shear angles in basal, mid-ventricular, and apical region of the LV.  $*p < 0.05$ . (Zhang et al., 2018)**

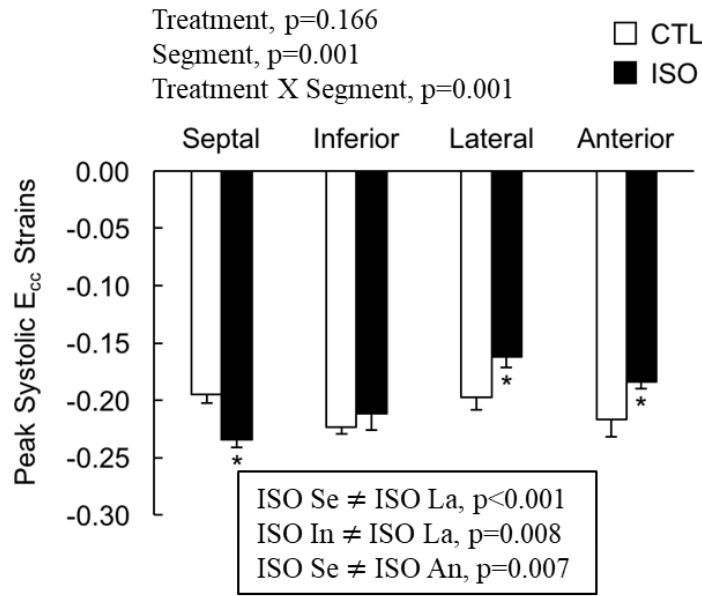
	Base		Mid-LV		Apex	
	Baseline	Iso	Baseline	Iso	Baseline	Iso
$E_{cc}$	$-0.19 \pm 0.01$	$-0.18 \pm 0.00$	$-0.21 \pm 0.01$	$-0.19 \pm 0.01$	$-0.19 \pm 0.01$	$-0.19 \pm 0.01$
$E_{ll}$	$-0.15 \pm 0.00$	$-0.11 \pm 0.01^*$	$-0.16 \pm 0.01$	$-0.15 \pm 0.01$	$-0.14 \pm 0.01$	$-0.14 \pm 0.01$
$E_{rr}$	$0.46 \pm 0.02$	$0.55 \pm 0.02^*$	$0.54 \pm 0.02$	$0.66 \pm 0.02^*$	$0.45 \pm 0.04$	$0.66 \pm 0.02^*$
$E_{cl}$	$0.04 \pm 0.00$	$0.08 \pm 0.01^*$	$0.05 \pm 0.00$	$0.09 \pm 0.01^*$	$0.00 \pm 0.01$	$0.06 \pm 0.00^*$
$E_{rl}$	$0.09 \pm 0.00$	$0.09 \pm 0.01$	$-0.05 \pm 0.01$	$0.00 \pm 0.02$	$-0.17 \pm 0.01$	$-0.14 \pm 0.02$
$E_{rc}$	$-0.05 \pm 0.00$	$-0.07 \pm 0.01^*$	$0.04 \pm 0.00$	$0.04 \pm 0.01$	$0.09 \pm 0.01$	$0.16 \pm 0.01^*$
CL Shear Angle (degree)	$7.47 \pm 0.38$	$12.70 \pm 1.10^*$	$9.09 \pm 0.51$	$14.92 \pm 0.73^*$	$1.36 \pm 0.91$	$9.99 \pm 0.66^*$

### 2.3.2 Regional Differences of Peak Circumferential Strain in the LV Mid-ventricle

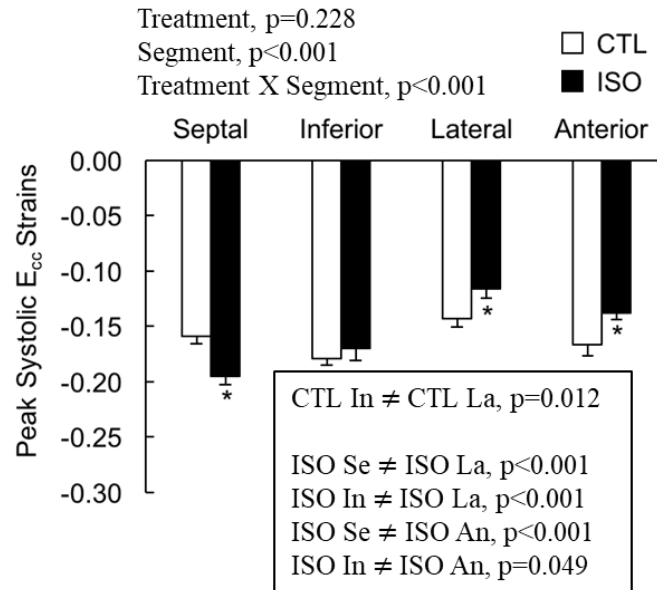
The regional effect of isoproterenol on the mid-ventricular peak circumferential strain in the LV was studied. The circumferential strain was compared over each myocardial segment and over each myocardial layer between the baseline and isoproterenol-infused cases. Results are summarized in Figure 2.6. Decrease in peak  $E_{cc}$  was found in all regions except the septal one. Specifically, significant decrease in peak  $E_{cc}$  was found in both the lateral and anterior regions. During systole, a shortening perimeter of myocardium was implied by negative and decreasing circumferential strain  $E_{cc}$ .



(a) *Endo*



**(b) Mid**



**(c) Epi**

**Figure 2.6: Effects of isoproterenol on peak systolic  $E_{cc}$  strains in different myocardial regions of mid-ventricle.** Peak systolic  $E_{cc}$  values were averaged over each segment of sub-endocardium (A, Endo), mid-myocardium (B, Mid), and sub-epicardium (C, Epi). The text above each figure shows  $p$  values for the main statistical effects. Significant differences between CTL and ISO groups, tested separately for each segment, are indicated by asterisks ( $*p<0.05$ ). Significant differences among the four segments, tested separately for untreated (CTL) and isoproterenol-treated (ISO) rats, are listed in the inset box. (Zhang et al., 2018)

## 2.4 Comparison between 2D and 3D Strain Analysis

Since isoproterenol is a  $\beta$ -adrenergic agonist (non-selective), the effect of another  $\beta$ -adrenergic agonist, dobutamine (cardio-selective), on LV function is worth mentioning here. A previous study using 2D Strain Analysis (DENSE) demonstrated an increase in peak  $E_{cc}$  in all regions (Zhong and Yu, 2010b). Specifically, a significant increase was found primarily in the septal, lateral, and anterior regions. Moreover, these isoproterenol-infused animals exhibited enhanced LV contraction and relaxation, reflected as increased maximum rates of LV pressure rise and fall (shown in Table 2.2), which is in line with previous reports on isolated murine hearts (Grieve et al., 2004) and/or conscious canine LVs (Karlner et al., 1977). Therefore, an expectation can be fairly made on  $E_{cc}$  that an increase would be found in  $E_{cc}$  under isoproterenol stimulation.

When 3D DENSE MRI was first proposed, a correlation study was done between strain results using 2D and 3D DENSE in healthy humans (Zhong et al., 2010). A large difference was found in  $E_{rr}$ , regardless of a small difference found in  $E_{cc}$ . As a matter of fact, the variation in strain difference can be explained from the perspective of continuum mechanics.

The equation for  $E_{cc}$  in 3D strain analysis can be derived as:

$$E_{cc} = \frac{1}{2}(F_{cc}^2 + F_{rc}^2 + F_{lc}^2 - 1) \quad (2.1)$$



where  $F_{cc}$ ,  $F_{rc}$ , and  $F_{lc}$  are the normal and shear components in the deformation gradient tensor in polar coordinates  $\underline{F}_{polar}$ , respectively. And the deformation gradient tensor  $\underline{F}_{polar}$  can be acquired by the following equation:

$$\underline{F}_{polar} = R\underline{F}R^T = \begin{bmatrix} F_{rr} & F_{rc} & F_{rl} \\ F_{cr} & F_{cc} & F_{cl} \\ F_{lr} & F_{lc} & F_{ll} \end{bmatrix} \quad (2.2)$$

where the rotation tensor  $R$  and the deformation gradient tensor  $\underline{F}$  in Cartesian coordinates are defined in Equation (1.4) and Equation (1.8), respectively.

In terms of in-plane strain, any of the longitudinal-related components of deformation should not be taken into account, which means  $F_{lc}$  is taken away from the equation of  $E_{cc}$  in 2D strain analysis. The equation for  $E_{cc}$  in 3D strain analysis can be defined as:

$$E_{cc} = \frac{1}{2}(F_{cc}^2 + F_{rc}^2 - 1) \quad (2.3)$$

where  $F_{cc}$  and  $F_{rc}$  are the normal and shear components in the deformation gradient tensor in polar coordinates  $\underline{F}_{polar}$ , respectively.

Subsequently, a 2D strain analysis was performed on  $E_{cc}$  and an increase was found in  $E_{cc}$  due to isoproterenol (shown in Figure 2.7). Likewise, similar increases induced by another  $\beta$ -adrenergic agonist (dobutamine) were demonstrated using 2D DENSE (Vandsburger et al., 2012; Zhong and Yu, 2010b) and 2D HARP (Li and Yu, 2010)

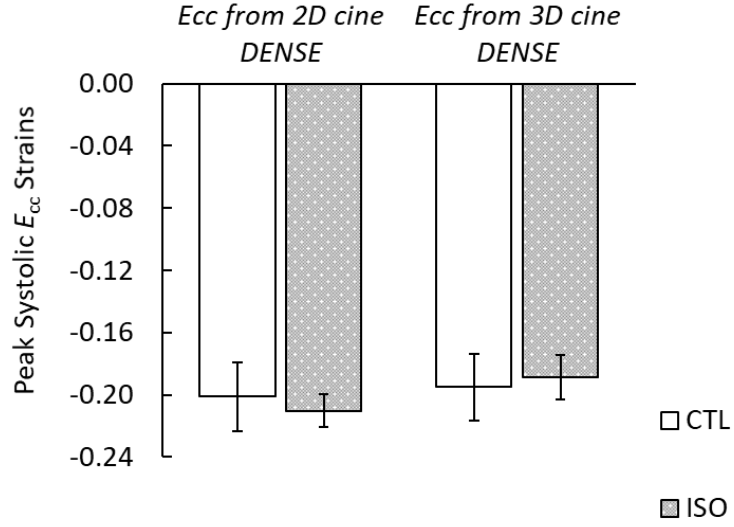


**Figure 2.7: Comparison in  $E_{cc}$  between 2D and 3D Strain Analysis**

However, as shown in Equation (2.1),  $F_{lc}$  in the equation for  $E_{cc}$  in 3D strain analysis can have a substantial influence. It has been significantly increased under isoproterenol stimulation in the present study (shown in Figure 2.8). More importantly, when a positive term  $F_{lc}$  (shown in Figure 2.8) was added to a negative  $E_{cc}$  in 2D strain analysis (shown in Figure 2.7), a decrease induced by  $\beta$ -adrenergic agonist (isoproterenol) was demonstrated (shown in Figure 2.7), which means the trend was completely reversed.

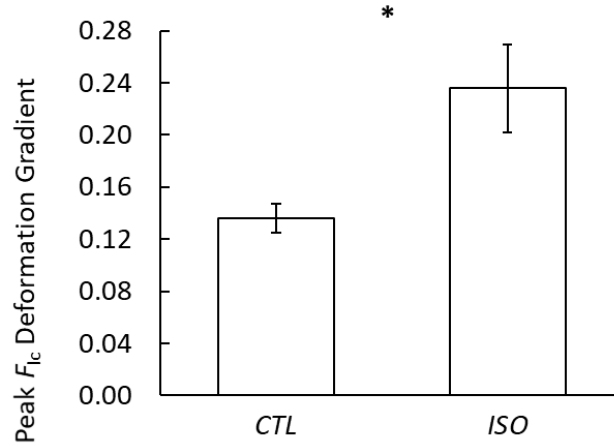


**Figure 2.8: Effect of isoproterenol on peak deformation gradient shear component  $F_{1c}$ .**

$*p < 0.05$ .

In conclusion, when 2D strain analysis was performed in SA view, the effect of the disease or treatment on longitudinal-related deformation could not be captured, while the information of circumferential-related deformation caused by the disease or treatment would not be lost under 2D strain analysis in LA view. In these two circumstances, potentially false values could be acquired in 2D strain results, and a totally opposite effect of disease or treatment could be reported on ventricular deformation. Previous studies have shown that a reduced  $E_{11}$  was significantly correlated with high mortality in patients with PH (Fine et al., 2013a). Under certain circumstances, if  $E_{11}$  in the patients with PH and corresponding treatment was found back to normal in the 2D strain analysis, a false

statement could be made that the treatment is working, while the patients are actually still in danger.

In the future, if the strain from MRI is used as an index in disease diagnosis, the present comparison results can facilitate the decision made by clinicians on the choice of a 2D or 3D scan protocol.

## **2.5 Conclusion**

Displacement ENcoding with Stimulated Echoes (DENSE) cardiac magnetic resonance (CMR) images are used to non-invasively capture the deformation of rat hearts. Myocardial contours were drawn based on short-axis and adjusted based on long-axis CMR images. Tools written in MATLAB were developed for the adjustment of myocardial contours. 3D DENSE Plugin for Crescent Organ (Liu, 2018) was developed for the application of the 12-segment model, and allowing user-defined meshing and noise suppression. In addition, a detailed profile of regional cardiac mechanics was created with it. Strains in rat left ventricles at baseline and under isoproterenol stimulation were compared statistically using an unpaired Student's t-test. Isoproterenol alters the cardiac mechanics (i.e., Lagrangian strains and torsion) of healthy rats in a region dependent manner, but the degree of the regional dependency varied among the Lagrangian strains and torsion. A significant increase in radial wall thickening ( $E_{rr}$ ), circumferential shortening ( $E_{cc}$ ), and longitudinal shortening ( $E_{ll}$ ) are found in the septum, indicating isoproterenol has

a more significant impact on the mechanical deformations of myocardium in the septum than in the free wall. Additionally, isoproterenol significantly increased peak systolic torsion throughout the LV wall, which is believed to be the main contributor to the significant increase in ejection fraction.

Regional differences may provide a reference for understanding the effects of inotropic agents on regional cardiac function, and provide insight for the development of targeted pharmaceutical therapies. For example, if a stress test identifies that a particular region does not experience an increase in torsion, then a specific treatment may be used to target that region.

### **3 Quantification of Regional Right Ventricular Strain in Healthy Rats using 3D Spiral Cine DENSE MRI**

#### **3.1 Background**

According to the report of the American Heart Association in 2011, 5.7 million Americans suffered from Congestive Heart Failure (CHF) (American Heart Association, 2011). In addition, pulmonary dysfunction is also frequently found with right ventricular dysfunction in heart failure (Robaeys et al., 2017). Particularly, pulmonary hypertension (PH) with right ventricular heart failure (HF) is very common among people older than 75. More importantly, an increasing number of studies have pointed out clinically relevant outcomes can be predicted based on the abnormalities in RV.

First of all, abnormalities in organ-level cardiac function of RV can serve as predictors of disease presence. An impaired right ventricular EF was found with significantly increased mortality in patients with CHF and coronary artery disease (Polak et al., 1983). And an impaired RIGHT ventricular ED volume was also found to be significantly correlated with the presence of arrhythmogenic right ventricular cardiomyopathy (ARVC) (Vigneault et al., 2016), and a significant higher mortality was reported in patients with dilated RV cavities (Sun et al., 1997).

Furthermore, abnormalities in right ventricular deformation are critical biomarkers for the management of cardiovascular diseases. Clinical studies (Derrick et al., 2001; Eyskens et al., 2004) have shown that reduced right ventricular deformation is an important marker

of global cardiac dysfunction for the patients after surgeries. In particular, a significant decrease was found in both right ventricular peak longitudinal and circumferential strains not only globally but also regionally in the patients with ARVC compared with control subjects (Vigneault et al., 2016). Besides, right ventricular free wall (RVFW) longitudinal peak systolic strain was reported to be a sensitive indicator of deterioration in RV of the patients with tetralogy of Fallot (TOF) (Scherptong et al., 2009). It was also used to assess the survival rate of the patients with PH (Fine et al., 2013a) and predict heart failure, especially for the HF with preserved reduced ejection fraction (Morris et al., 2017). As for the patients with pulmonary arterial hypertension (PAH), upcoming right-sided heart failure, clinical deterioration, and patient mortality can be forecasted through RV longitudinal peak systolic strain (Sachdev et al., 2011). Since RV dysfunction in the patients with PAH has a high mortality rate (Ryan et al., 2015), abnormalities in right ventricular deformation should be an important focal point during the management of PAH.

The rat model is widely used in cardiac research on RV. For example, recent studies have used rats with PH and right ventricular HF to investigate remedies for PH (Labinskyy et al., 2008; Mouchaers et al., 2010; Sawamura et al., 2009). Since impaired right ventricular longitudinal and circumferential strains have been frequently reported to be strongly correlated with the presence of cardiovascular diseases, establishing reproducible baselines of these strains is essential, and could be used for assessment of the effectiveness of various treatments. Compared with MRI, the conventional echocardiographic imaging,

such as velocity vector imaging and speckle tracking imaging, underestimated longitudinal strain (Fine et al., 2013b). Regarding MRI technique, standard Spatial Modulation of Magnetization (SPAMM) tagged MRI was initially used to evaluate RV deformation (Haber et al., 2000). However, the RV free wall is normally 3 to 4 times thinner than the LV free wall (Matsukubo et al., 1977), making tracking the entire lengths of the tags extremely difficult, then resulting in underestimated strains. Aside from SPAMM, cine Steady State Free Precession (SSFP) MRI with feature tracking was also used to quantify RV strains (Lollert et al., 2018; Nucifora et al., 2016; Sachdev et al., 2011). But the strains acquired from SSFP were much less reproducible than those from DENSE. For instance, the inter-observer coefficients of variation (CoV) for RV longitudinal and circumferential strains at 3T using SSFP are ~30% globally and ~47% segmentally (Schuster et al., 2013), compared with those of ~3% globally and ~10% segmentally using DENSE (Suever et al., 2017). Unfortunately, there are very limited studies conducted on the right ventricle with DENSE MRI, especially no published study using rat model and DENSE MRI. Therefore, the current study investigated the normal state of cardiac mechanics in rat RV, in order to establish a baseline for deformation in a healthy heart.

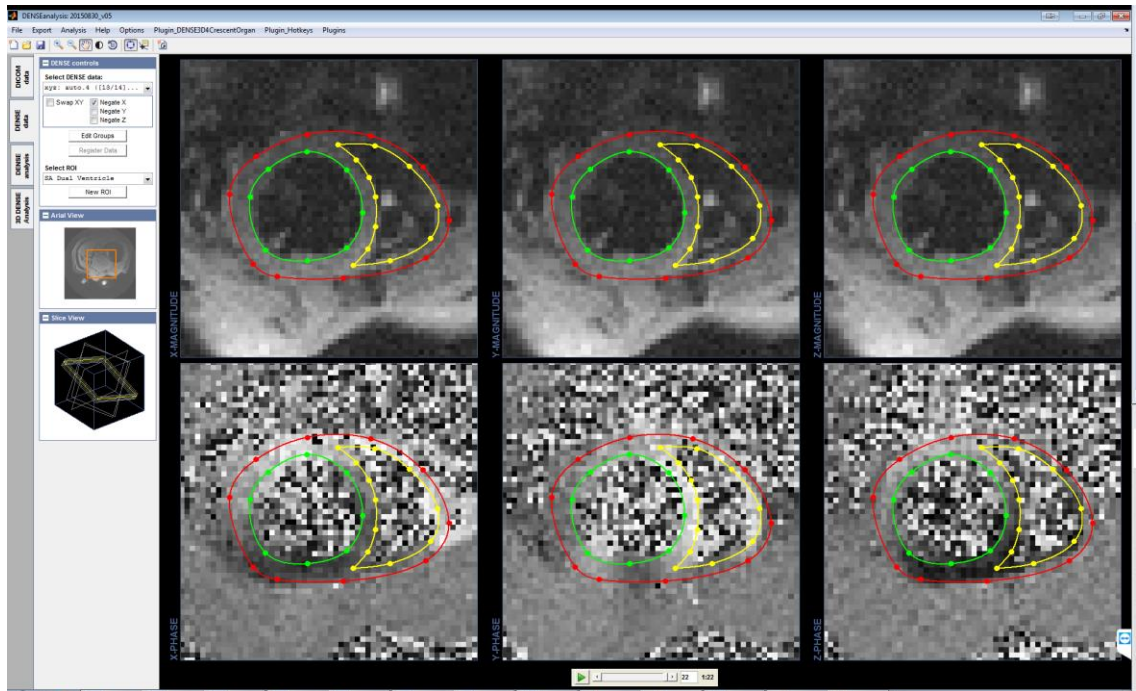


## **3.2 Methods**

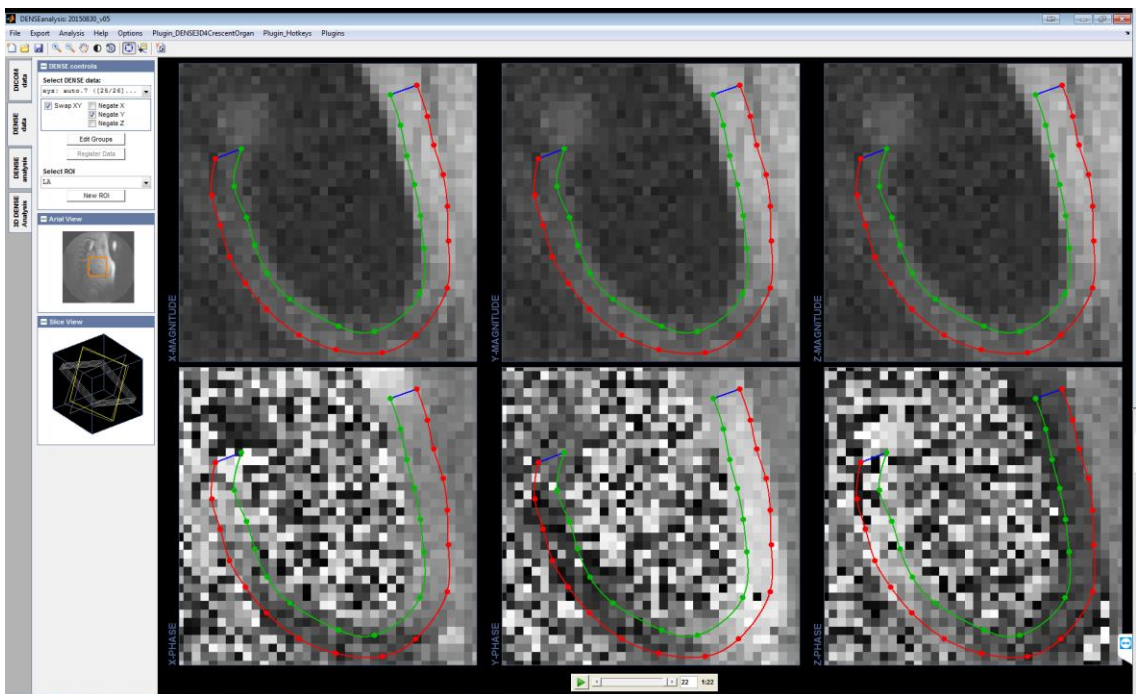
### **3.2.1 Myocardial Segmentation**

The DENSE CMR images acquired by Dr. Xiaoyan Zhang on the healthy rats (Zhang et al., 2017) were used in this study. And images of 7 healthy female Sprague-Dawley rats were analyzed, since the RV could not be resolved on the CMR images of the remaining 3 healthy rats.

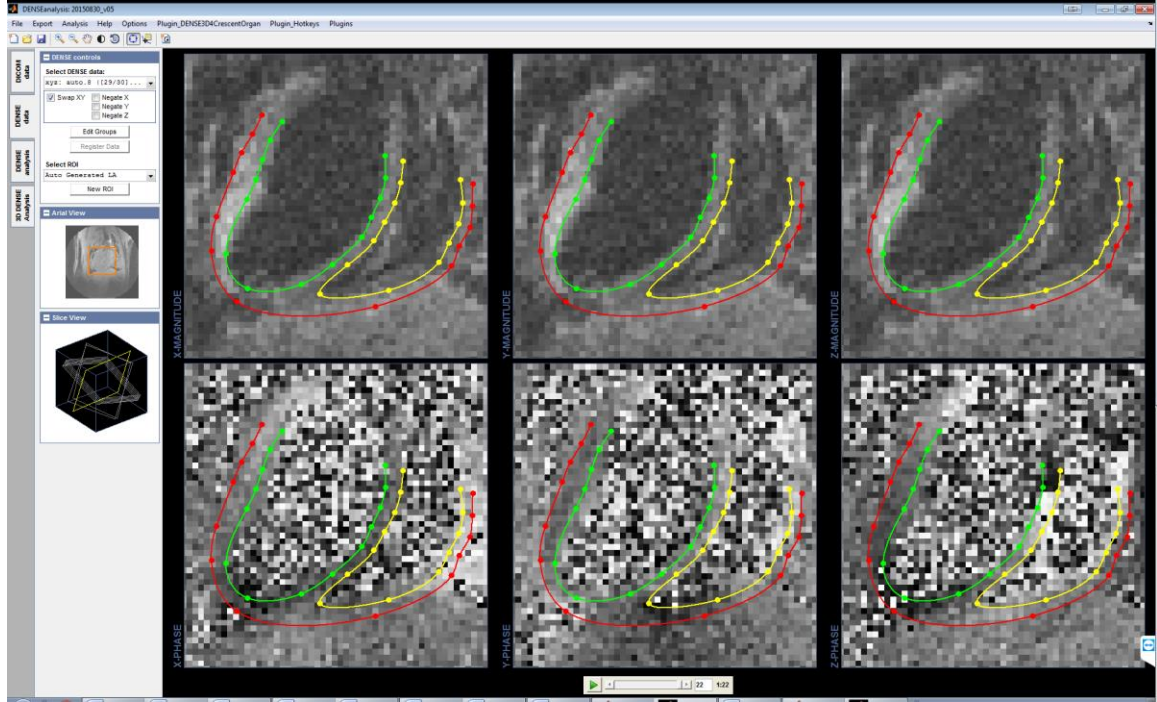
The RV free wall was segmented from the blood pool using DENSE3D Plugin (Suever, 2016), a plugin in DENSEanalysis which is capable of dealing with biventricular contours. The same methodology employed in Chapter 2.2.1 was used for RV segmentation. Biventricular endocardial and epicardial borders were traced over the whole cardiac cycle manually on SA views (shown in Figure 3.1a), but automatically on VLA (2-chamber) (shown in Figure 3.1b) and HLA (4-chamber) views (shown in Figure 3.1c) using the custom scripts mentioned in the Chapter 2.2.1.



(a) *Short-axis contours viewed from the apex*



(b) *Vertical long-axis contours*



(c) *Horizontal long-axis contours*

**Figure 3.1: Biventricular contours at end diastole of mid-ventricle.** Images were taken on Aug. 30, 2015. Red curves are epicardial contours. Green curves are LV endocardial contours. Yellow curves are RV endocardial contours.

### 3.2.2 3D Anatomical Contours

Although SSFP has been considered as the standard method for imaging the anatomy of the heart, a recent study pointed out that the off-resonance artifacts would be noticeable if the SSFP was used with high field strength (7 Telsa in present study) (Berr et al., 2005). During our DENSE CMR scan, despite having 5-6 SA slices that cover near 80% of the end-systolic ventricular length, they only cover 60% of the end-diastolic ventricular length

due to atrioventricular plane displacement (AVPD) (blue curves in Figure 3.2). In order to reconstruct the animal-specific biventricular anatomy along the full ventricular length with a limited number of SA slices, extra approximated SA slices (black curves in Figure 3.2) near apex were created using the SA and LA contours (shown in Figure 3.1) in a custom script embedded in the 3D DENSE Plugin for Crescent Organ (Liu, 2018).

First of all, the drawn SA and LA contours were transformed from the image coordinate system to the global coordinate system. Since the contours on each slice are stored in pixel coordinates (shown in Figure 3.1), they were converted to the global coordinate system using the information of volumetric pixels (voxels) size, slice location, and slice orientation stored in the tags of DICOM (blue and red curves in Figure 3.2).

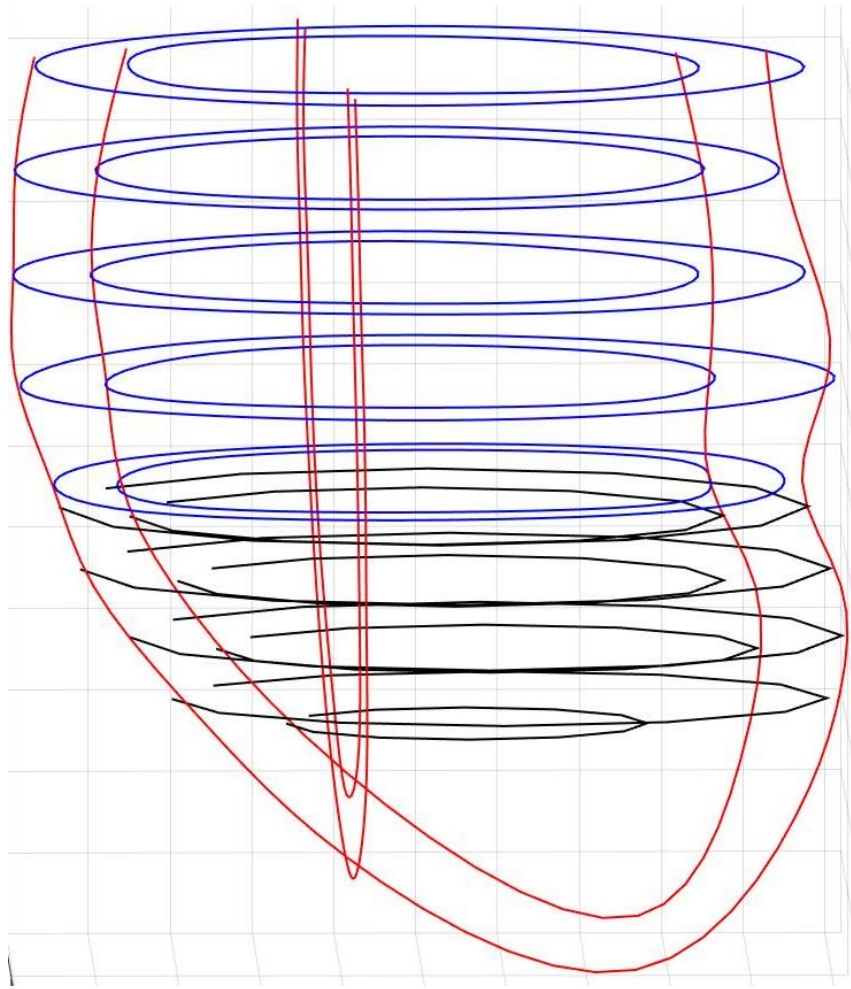


**Figure 3.2:** *Converted end-diastolic contours of all slices are gathered in the global coordinate system. Blue curves are SA contours. Red curves are LA contours. Black curves are approximated SA contours.*

After the drawn SA and LA contours were placed together, the apical approximated SA contours (black curves in Figure 3.2) were generated. Specifically, fitted points (black diamond dots in Figure 3.3) were created by using a plane to intersect the drawn SA and LA contours in a specific longitudinal location of interest. Assuming the apical SA contours

(the red curve in Figure 3.3) have an elliptical shape, they were generated by approximating the fitted points using Brent-Powell minimization method (shown in Figure 3.3).

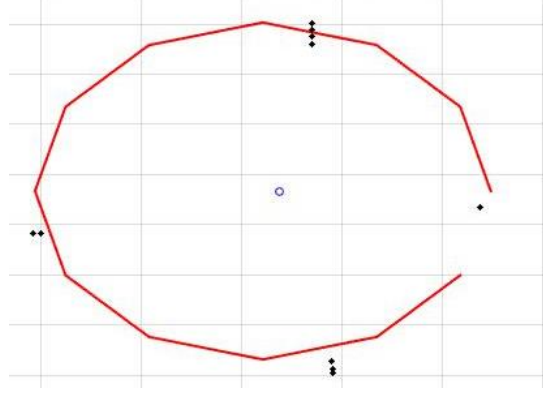


**Figure 3.3: An apical SA contour is approximated with the points in two LA contours.**

*Red curve is the apical SA contour. Black points are from LA contours.*

### 3.2.3 Discretization of Biventricular Surfaces

As depicted in Figure 3.4, the 3D end-diastolic epicardial, LV endocardial, and RV endocardial surface meshes were created from the converted end-diastolic contours of all slices (shown in Figure 3.2) using the surface mesh generation method developed by Haggerty et al. (2014) for human ventricles in DENSE3D Plugin (Suever, 2016).



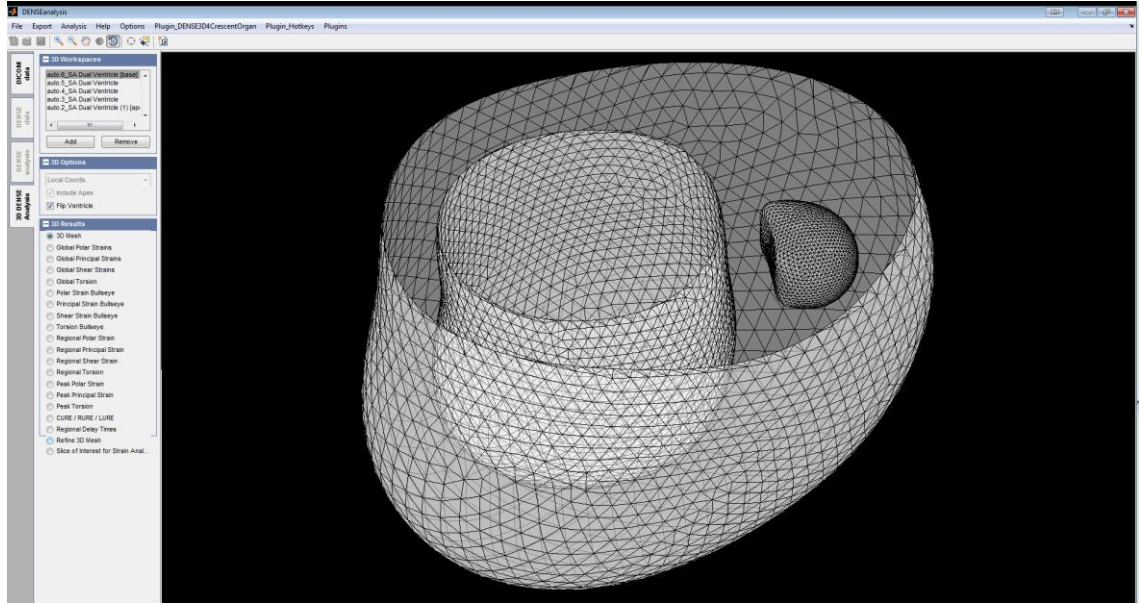


***Figure 3.4: End-diastolic biventricular meshes created with DENSE3D Plugin***

However, as pictured in Figure 3.4, the plugin failed to fit the RV endocardial mesh into the right ventricle of small animals like murine, which have a much more crescent-shaped cavity (blue curves in Figure 3.5) and are sharper at the RV insertion point.

In order to get a better RV endocardial mesh at end diastole, an iteration algorithm was developed for adjusting the RV surface mesh into its actual crescent shape. Firstly, the pre-generated RV endocardial mesh was relocated inside the converted end-diastolic SA contours (blue curves in Figure 3.6). Subsequently, the RV generation module in DENSE3D Plugin (Suever, 2016) was run repeatedly with input parameters varying in values.. The parameters were varied in each iteration but within specified ranges until the minimal sum of distances from the points on each SA contour to RV mesh surface was reached. Eventually, the best setting of the input parameters for RV generation was attained for each specific animal. The algorithm was integrated into the 3D DENSE Plugin for

Crescent Organ (Liu, 2018), making the plugin capable of handling the heart in which the biventricular shape is sharper at the right ventricle insertion points. Eventually, the epicardial mesh (green surface in Figure 3.6) and LV endocardial mesh (blue surface in Figure 3.6) were loaded with a refined RV mesh (red surface in Figure 3.6) in 3D DENSE Plugin for Crescent Organ.

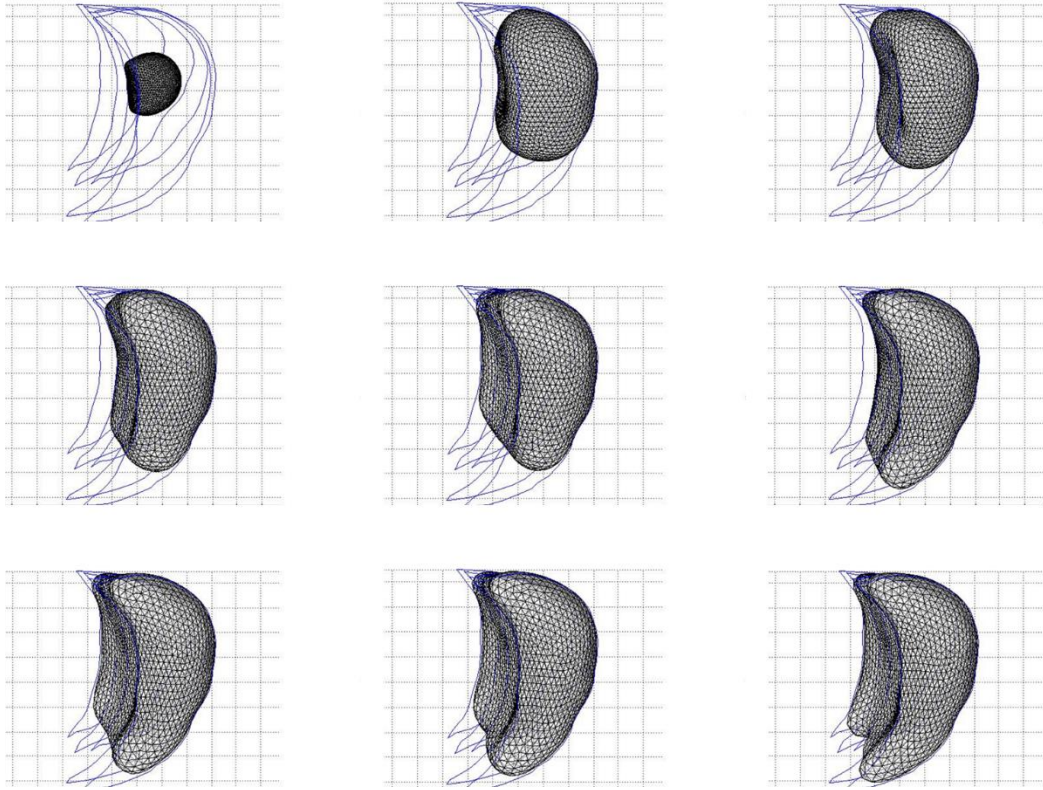


**Figure 3.5: Refinement for end-diastolic RV endocardial mesh.** Blue curves are a stack of converted end-diastolic SA contours.



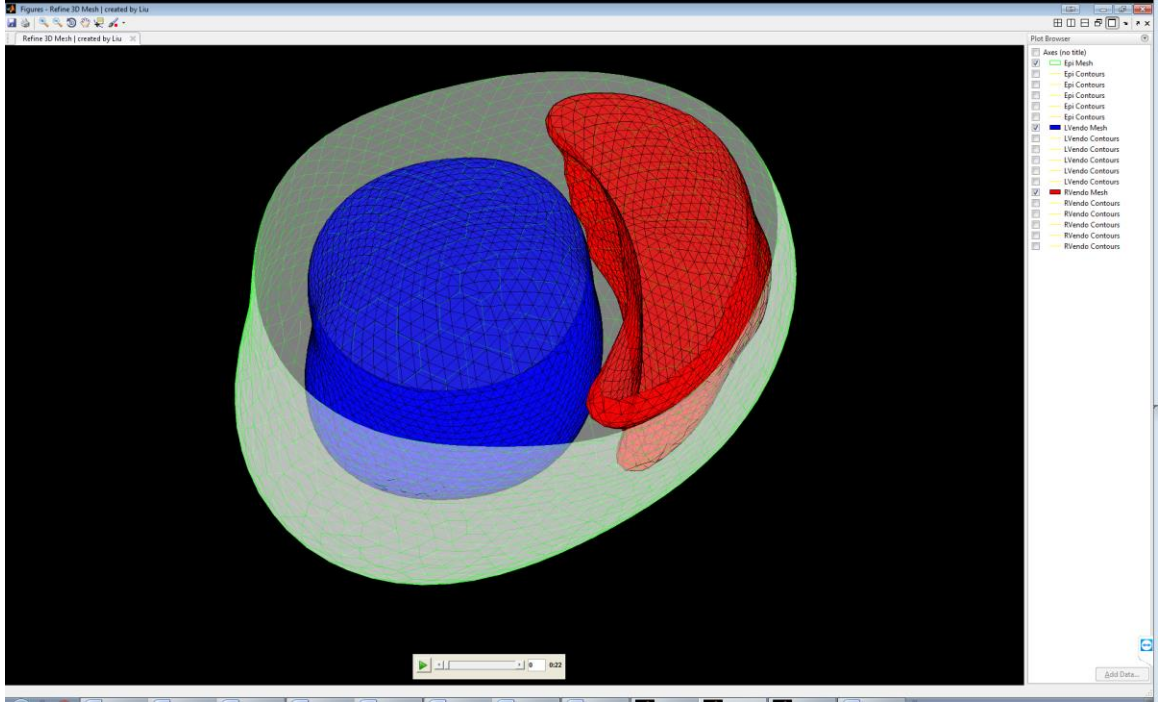


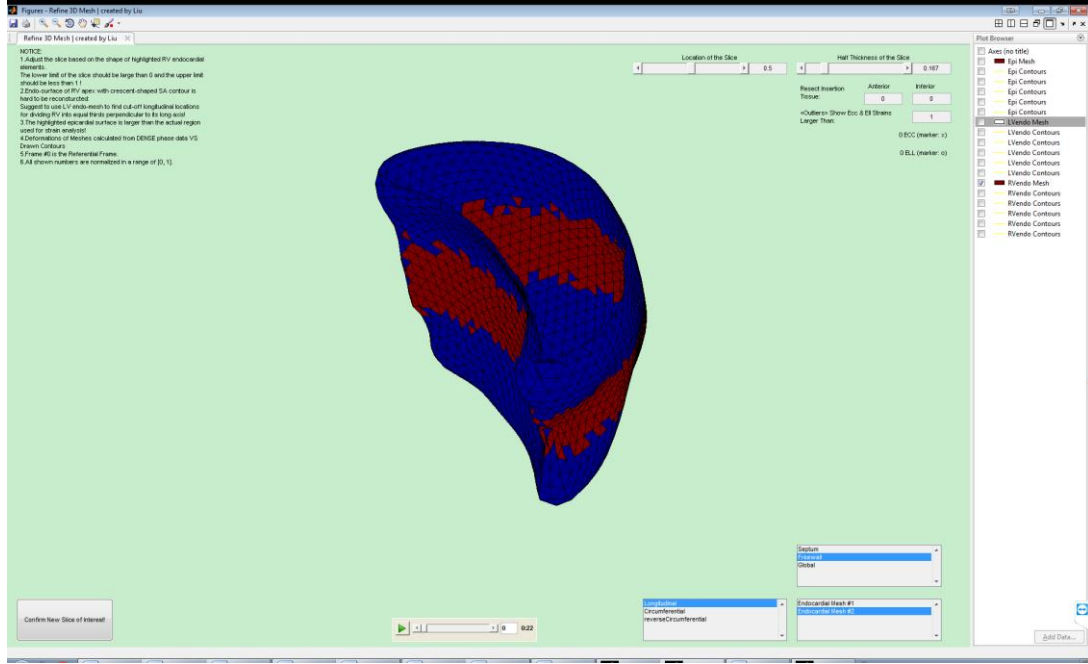
***Figure 3.6: End-diastolic biventricular meshes with a refined RV mesh***

### **3.2.4 Lagrangian Strains Analysis**

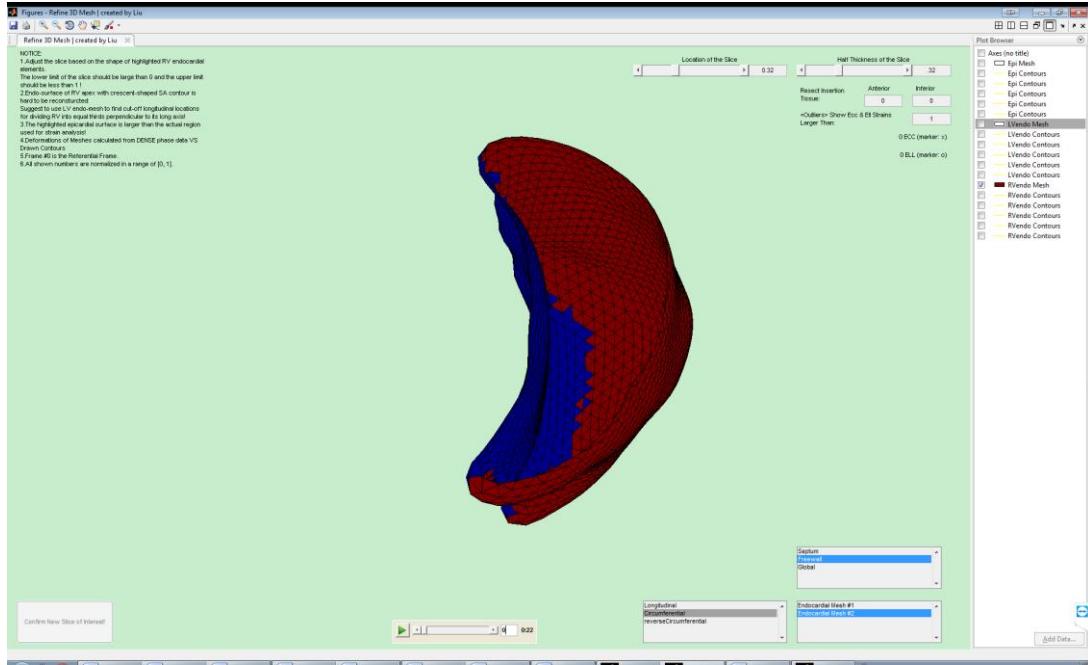
3D Lagrangian displacements were retrieved at each voxel of phase images by unwrapping the phase images (Spottiswoode et al., 2007). More strain points were interpolated into the voxels to acquire the 3D Lagrangian displacement field over time fitted by linear radial basis functions (Hardy, 1990). Afterward, the 3D Lagrangian strain tensor in Cartesian coordinates was computed at each strain point over time. Thereafter, a local coordinate system was created at each element of LV and RV endocardial meshes and assigned to nearby strain points (Suever et al., 2017). Finally, the Lagrangian strain tensor in polar coordinates was derived by transforming the Cartesian strain tensor into the local

coordinate system at each strain point. Thanks to the local coordinate system which accounts for the complex shape of RV, the longitudinal and circumferential strains can be better resolved locally.

In order to average the strains from the same region of interest, the longitudinal and circumferential positions of each strain point were normalized and then parameterized (Suever et al., 2017). The longitudinal parameterization was performed by a longitudinal parameterization module in DENSE3D Plugin (Suever, 2016) (depicted in Figure 3.7a). The circumferential parameterization was improved by accounting for the fact that the anterior and inferior insertions of the RV to the LV shift circumferentially along the ventricular long axis. Circumferential parameterization was performed twice in the 3D DENSE Plugin for Crescent Organ (Liu, 2018) for longitudinally varying anterior and inferior RV insertions, respectively. As a result, right ventricular free wall was precisely segmented from left ventricular free wall or the interventricular septum (depicted in Figure 3.7b).



*(a) Longitudinal segmentation for the RV middle slice (Red region)*



*(b) Circumferential segmentation for the RV free wall (Red region)*

**Figure 3.7: Biventricular longitudinal and circumferential segmentation**

Furthermore, a 12-segment model is applied to the RV free wall (depicted in Figure 3.8) and segment names are summarized in Table 3.1. Specifically, the RV free wall was

divided into circumferential fourths (anterior, anterolateral, inferolateral and inferior segments) and longitudinal thirds (basal, middle, and apical segments). The anterior and inferior segments also include a part of the RV outflow tract and a part of the RV inflow tract (depicted in the Figure 3.9) which are usually included in the RV segmentation model in LA views (Auger et al., 2012; Hurst, 1988).

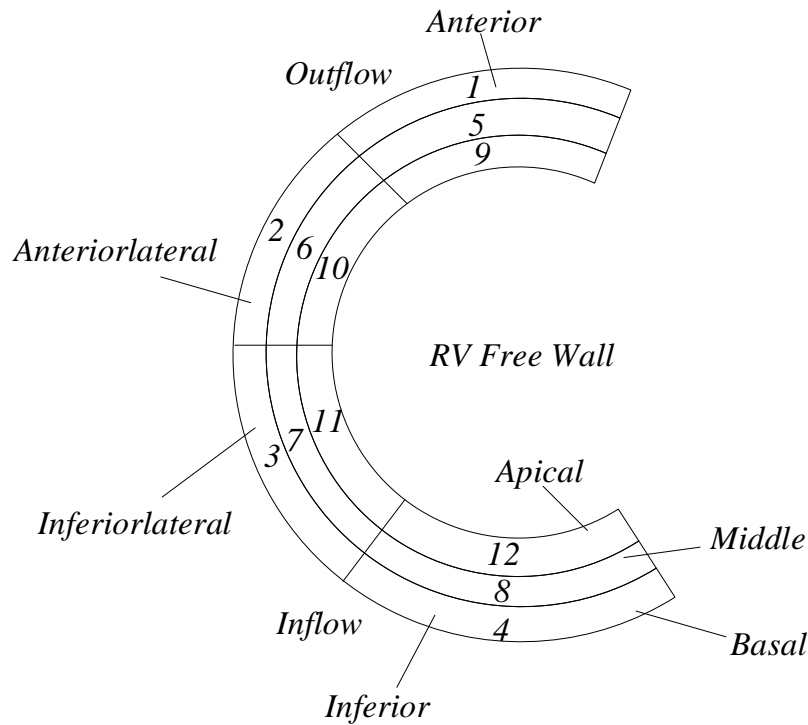


**Figure 3.8: A 12-segment model at RV free wall**

**Table 3.1: Notation of segments in RV free wall**

Anterior segments	Anterolateral segments	Inferolateral segments	Inferior segments
1. Basal anterior	2. Basal anterolateral	3. Basal inferolateral	4. Basal inferior
5. Middle anterior	6. Middle anterolateral	7. Middle inferolateral	8. Middle inferior
9. Apical anterior	10. Apical anterolateral	11. Apical inferolateral	12. Apical inferior

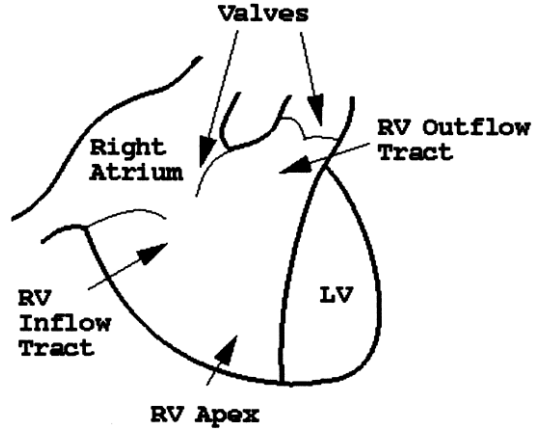


*Figure 3.9: RV segmentation model in LA view (Hurst, 1988)*

### 3.2.5 Statistical Analysis

All data are presented as mean  $\pm$  standard deviation. Comparisons between 4 groups were performed using one-way ANOVA with Student's *t*-tests, while comparisons between 2 groups were conducted with unpaired Student's *t*-test assuming equal variances. A value of  $p < 0.05$  was considered significant.

## 3.3 Result

### 3.3.1 Distribution of Peak Systolic Strains at Base and Mid-ventricle of RV

Peak strains at base and mid-ventricle of RV are represented in Figure 3.10. There was no significant difference both in peak circumferential strain ( $E_{cc}$ ) and peak longitudinal strain ( $E_{ll}$ ) between base and middle segments of the RV free wall. At base, no differences were noted between peak circumferential strain ( $E_{cc}$ ) and peak longitudinal strain ( $E_{ll}$ ).

However, peak circumferential strain ( $E_{cc}$ ) was significantly higher than peak longitudinal strain ( $E_{ll}$ ) at mid-ventricle.

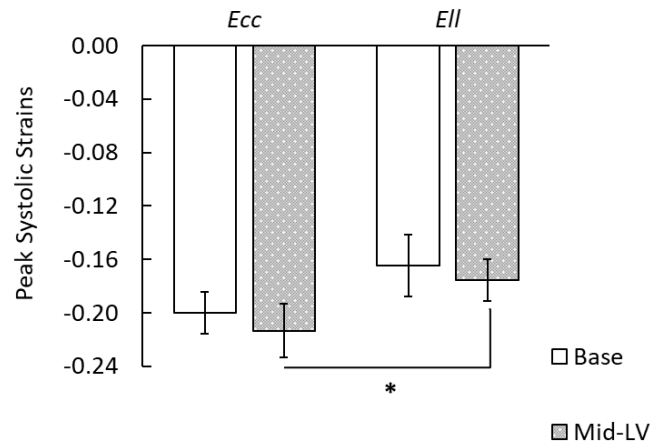


**Figure 3.10: Distribution of peak systolic strains at base and mid-ventricle of RV**

### 3.3.2 Distribution of Peak Systolic Strains in the RV Base

As presented in Figure 3.11a, no differences were found in circumferential strain ( $E_{cc}$ ) among the anterior, anterolateral, inferolateral, and inferior segments of the RV basal free wall. Nevertheless, longitudinal strain ( $E_{ll}$ ) in the RV basal free wall was significantly lower in anterior segment compared to anterolateral, inferolateral, and inferior segments, respectively (Figure 3.11b).

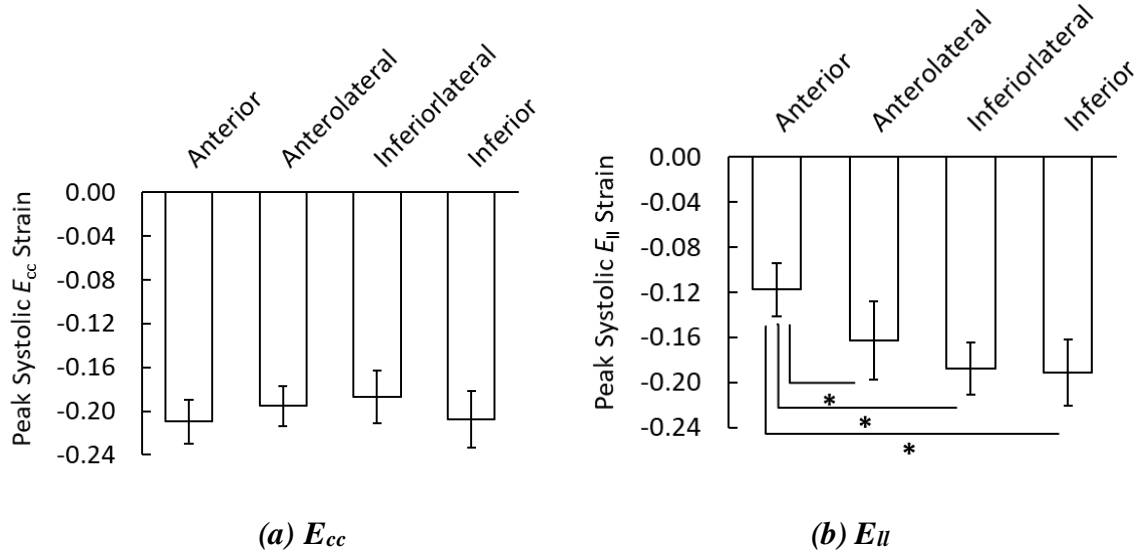


**Figure 3.11: Distribution of Peak Systolic Strains in the RV Base**

### 3.3.3 Distribution of Peak Systolic Strains in the RV Mid-ventricle

Circumferential strain ( $E_{cc}$ ) exhibited similar peak systolic values in the anterior, anterolateral, inferolateral, and inferior segments of the RV middle free wall (Figure 3.12a). However, longitudinal strain ( $E_{||}$ ) in the RV middle free wall was significantly lower in anterior segment compared to anterolateral, inferolateral, and inferior segments, respectively (Figure 3.12b).

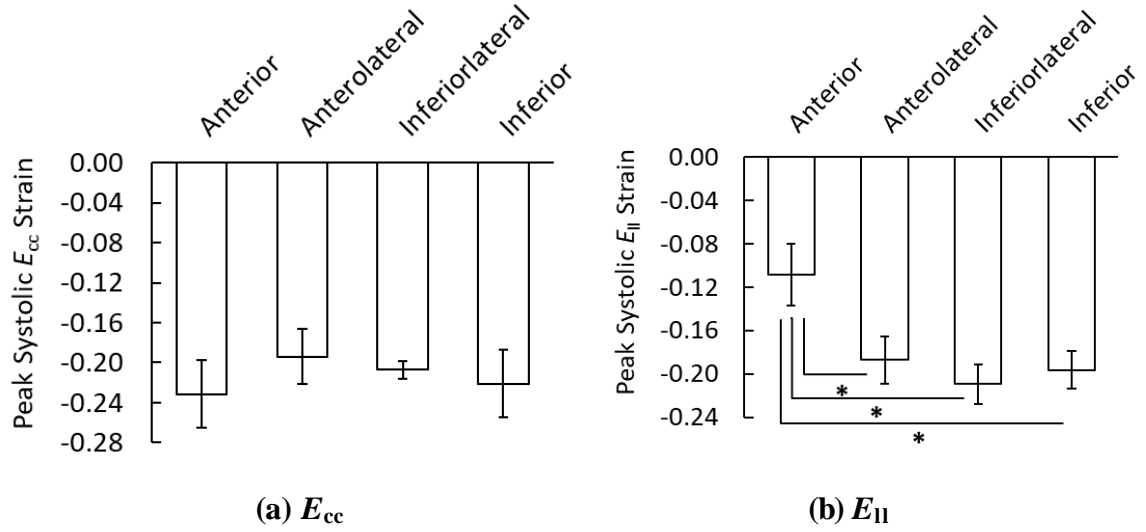


**Figure 3.12: Distribution of Peak Systolic Strains in the RV mid-ventricle**

### 3.4 Discussion

In the current study, the circumferential and longitudinal strains were investigated over the base and the mid-ventricle of the RV free wall of healthy rats.

The average peak circumferential strain ( $E_{cc}$ ) is  $-0.20 \pm 0.01$  at base and  $-0.21 \pm 0.02$  at mid-ventricle, which is in a good agreement with the previous study using DENSE ( $-0.19$  and  $-0.19$ , respectively) (Suever et al., 2017), and the strains resolved using strain-encoding (SENC) are  $-0.18$  and  $-0.18$ , respectively (Hamdan et al., 2008), and  $-0.20$  and  $-0.19$ , respectively (Youssef et al., 2008), consistent with the findings of the present study. Additionally, the average peak longitudinal strain ( $E_{||}$ ) is  $-0.16 \pm 0.02$  at base, which is in agreement with the value of  $-0.16$  reported by Fine et al. (2013b). In the current study, the mid-ventricle value was  $-0.18 \pm 0.02$ , which is consistent with the reported values of  $-0.18$



(Suever et al., 2017) and  $-0.18$  (Hamdan et al., 2008). Moreover, peak circumferential strain ( $E_{cc}$ ) is significantly higher than peak longitudinal strain ( $E_{ll}$ ) at mid free wall ( $-0.21 \pm 0.02$  vs.  $-0.18 \pm 0.02$ ,  $p < 0.002$ ). It indicates that circumferential shortening predominates over longitudinal shortening in the myocardial deformation of RV middle free wall, as was also the case ( $-0.23$  vs.  $-0.15$ ,  $p < 0.001$ ) in the study of Pettersen et al. (2007) who used tagged MRI.

The present study also quantified the circumferential and longitudinal strains in the different circumferential segments of the RV free wall. First of all, no regional differences in the SA view were found for the peak circumferential strain ( $E_{cc}$ ) neither at base nor at mid-ventricle. This is consistent with the observation in healthy humans by Vigneault et al. (2016) who used SSFP to assess  $E_{cc}$  regionally. Furthermore, regional differences in longitudinal strain ( $E_{ll}$ ) were solely detected in the anterior segment not only at base but also at mid-ventricle of RV free wall. This finding can be elucidated in two perspectives.

From the perspective ventricular kinematic deformation, the significant difference in longitudinal strain estimated in the anterior segments resulted from the combination of LV and RV twists. The LV torsion was previously reported as positive CL shear angle at base and mid-ventricle (Rüssel et al., 2009; Zhang et al., 2017; Zhong et al., 2011). As positive torsion was defined as counterclockwise rotation when viewed from the apex (illustrated in Figure 3.1), the LV twisted toward the RV anterior segments at base and mid-ventricle. Considering a part of the RV outflow tract (depicted in the Figure 3.9) was included in the

basal and mid-ventricular anterior segments, the resistive role of the RV outflow tract was revealed in preventing the high pressure induced in the free wall from impairing the pulmonary artery which is sensitive to pressure (Armour et al., 1970). Resistance at the anterior side of RV was generated from the RV outflow tract against the LV twist toward RV. For one thing, the mechanism of longitudinal activation of RV free wall has been verified electrophysiologically (Meier et al., 1980), echocardiographically (Pettersen et al., 2007), and radiologically (Pettersen et al., 2007). The contraction of RV free wall starts at the apex, followed by a longitudinal propagation towards outflow tract. Since the resistance was primarily driven in the longitudinal direction, the regional difference was absent in circumferential strain. For another thing, the overall torsion is significantly lower in the RV compared to the overall LV torsion (Pettersen et al., 2007), indicating the body of RVFW was compliant with the motion of LV inferior wall which is consistent with the findings of the absent resistance in the body of RVFW (Armour et al., 1970). Thus, the significant difference was solely occurred at the anterior side instead of the body of RVFW. Additionally, the resistance at the anterior RVFW and the compliance in the body of RVFW were supposed to counteract on LV, resulting in regional difference in LV deformation between the anterior and inferior sides of LV. And this assumption is supported by the finding in previous studies on healthy rats that the torsion at mid-ventricle of LV was significantly lower at the anterior side compared to the inferior side ( $p < 0.0001$ ) (Zhang et al., 2017). Accordingly, the overall effect of withholding the longitudinal shape in the

anterior segments of the basal and mid-ventricular RVFW resulted in a significantly reduced longitudinal strain in those segments.

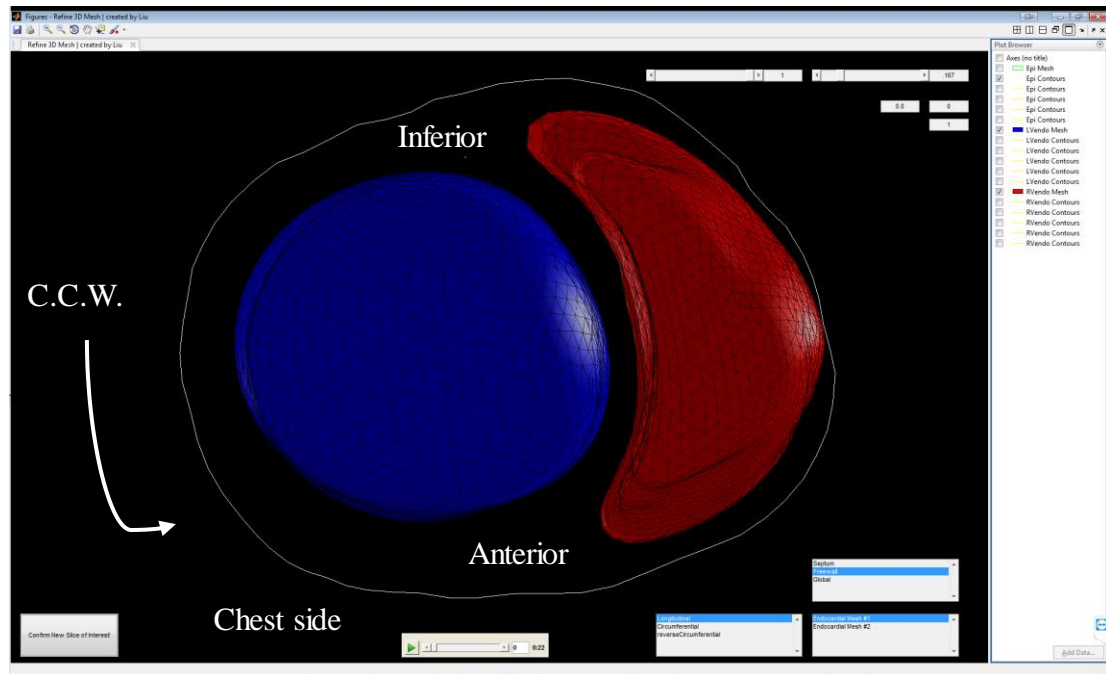


*Figure 3.13: Schematic of torsion direction as viewed from the apex.*

*White curve represents basal epicardial border.*

In the current study, most of the location points (black dots in Figure 3.14) with positive longitudinal strain (relaxation) at end systole were found near the anterior RV insertion site. Since the anterior septal insertion was inside the basal and mid-ventricular anterior segments, the complexity of the deformation at the RV insertions altered the average longitudinal strains in the anterior segments. Besides, either morphologic or physiologic differences have been discovered at the septal insertions in the RV myocardium under PH (Blyth et al., 2005; Sanz et al., 2007; Shehata et al., 2011), PAH (McCann et al.,

2007), and hypertrophic cardiomyopathy (Bravo et al., 2016). More importantly, previous study reveal that two septal regions vary in both fiber architecture and fiber compliance (Armour and Randall, 1970), which may explain the strain difference occurring at the anterior side but not the inferior side.

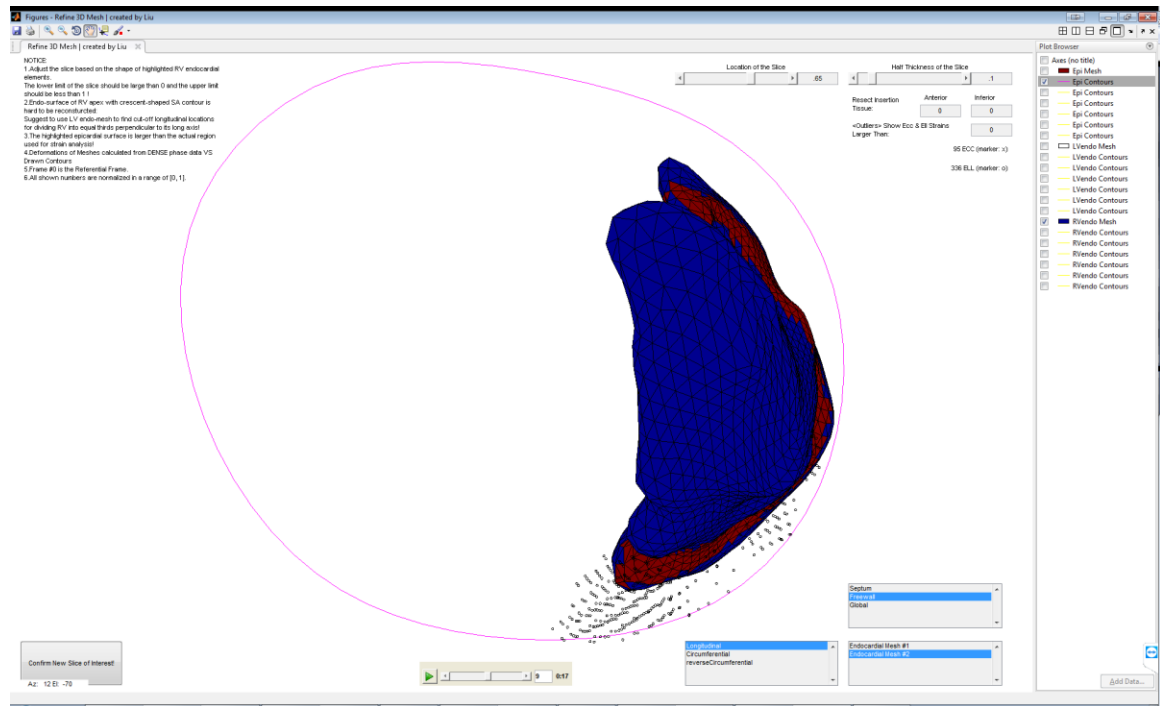


**Figure 3.14: Positive longitudinal strain values (black dots) found at end systole near the insertion of the rat RV scanned on Nov. 01, 2015.**

*Magenta curve represents basal epicardial border seen from the apex.*

Another point worth to be mentioned is that, at base and mid-ventricle, no significant differences in circumferential strain (MRI tagging) were found between the anterior and inferior RV insertions not only in healthy individuals but also in the patients with PH

(Shehata et al., 2011). More interestingly, at base and mid-ventricle, the longitudinal strain (SENC) was also reported to be lower in anterior RV insertion compared to inferior RV insertion in healthy RV, whereas the differences became significant under PH (Shehata et al., 2011). Accordingly, a significantly reduced longitudinal strain potentially existed at the anterior side of basal and middle RVFW in the control group but SENC was not sensitive enough to detect it. However, under PH, since the RV outflow tract (anterior free wall) resisted harder against the increased pressure in the pulmonary artery, the difference in longitudinal strain between the anterior and inferior RV insertions became so significant that SENC was adequate to detect it. On the other hand, the present findings imply the difference between the anterior and inferior RV insertions of healthy RV was significantly revealed in longitudinal direction of deformation by a highly reproducible technique for precise measurement (DENSE).

### **3.5 Limitations**

Since only normal rat RV was investigated, one limitation is that no observations were conducted on the RV with known cardiomyopathy or under treatments. Future work is to assess RV function in animals with cardiac dysfunction. The sample size was 7 animals in the current study. However, a smaller sample size (5) was used in the study on RV strains in pig (Zhang et al., 2013).

The 3D DENSE data was obtained by stacking multiple 2D SA slices with same thickness and orientation instead of a volumetric scan. As the orientation of SA slices was defined as the transmural direction of mid-ventricular septum, the orientation of the basal slice did not align with the transmural direction of basal septum. This resulted in blurring of the phase image in the apical slice, since more mixing between the displacements from blood pool and myocardium occurs near the ventricular border. Thus, the image quality of the apical slice was inadequate for resolving the RV strains.

Additionally, RV radial strain analysis was not included in the present study. This is due to the extremely thin wall in murine RV, which means an improved DENSE pulse sequence is required for higher spatial resolution with sufficient signal to noise. Thus, RV radial strain analysis, even the transmural difference in strains, will be a future focus.

However, cine DENSE CMR has been proven to have high inter-observer and inter-test reproducibilities in RV (Suever et al., 2017). Therefore, the drawbacks did not jeopardize the goal of the present study, which was mainly designed to use a highly objective method to provide a baseline reference of RV circumferential and longitudinal strains for future extensive studies using rat models to study heart disease and treatments.

### **3.6 Conclusion**

A preliminary study was performed on regional RV strains in the healthy rat heart using DENSE, a technique shown to have highly reproducible results in rodent (Haggerty et al.,

2013b). A detailed baseline profile of right ventricular circumferential and longitudinal strains was acquired non-invasively from DENSE CMR images. Average basal and mid-ventricular strains agree with the findings of previous studies (Fine et al., 2013b; Hamdan et al., 2008; Suever et al., 2017; Youssef et al., 2008). Despite no regional differences in peak circumferential strain, peak longitudinal strain exhibited regional difference both at base and at mid-ventricle, which could be related to the differences in LV and RV twists, mechanical activation of RVFW, and fiber structure and material response of two septal insertions.

### **3.7 Clinical Implications**

The normal state of cardiac mechanics in RV was investigated, which may serve as a baseline in prognostic information. Combining this with the conventional clinical variables can be used in a comprehensive evaluation for early detection of right ventricular dysfunction. By using a reliable noninvasive method, this approach may help to elucidate clinical risk factors from MRI for cardiovascular diseases.

## Appendices

### Appendix A – Abbreviations

ARVC	Arrhythmogenic Right Ventricular Cardiomyopathy
AV	Atrioventricular
AVPD	Atrioventricular Plane Displacement
CMR	Cardiac Magnetic Resonance
CHF	Congestive Heart Failure
CoV	Coefficient of variation
CSO	Contour Segmentation Objects
DENSE	Displacement ENcoding via Stimulated Echoes
DICOM	Digital Imaging and Communications in Medicine
Dob	Dobutamine
ECG	Electrocardiogram
ES	End Systole
ED	End Diastole
HLA	Horizontal Long-Axis
HARP	Harmonic Phase
HF	Heart Failure
LAD	Left Anterior Descending (Artery)
LCX	Left Circumflex
LV	Left Ventricle
MRI	Magnetic Resonance Imaging
PAH	Pulmonary Arterial Hypertension
PH	Pulmonary Hypertension
PVR	Pulmonary Valve Replacement
RV	Right Ventricle
RVEDV	Right Ventricular End-Diastolic Volume
RVEF	Right Ventricular Ejection
RVFW	Right Ventricular Free Wall
RVSV	Right Ventricular Stroke Volume
RCA	Right Coronary Artery
SA	Short Axis
SPAMM	Spatial Modulation of Magnetization
SNR	Signal-to-noise Ratio
SSFP	Steady State Free Precession
TOF	Tetralogy of Fallot
VLA	Vertical Long-Axis
WEM	Winged Edge Mesh



## References

- Aletras, A.H., Ding, S., Balaban, R.S., Wen, H., 1999. DENSE: Displacement Encoding with Stimulated Echoes in Cardiac Functional MRI. *Journal of Magnetic Resonance* 137, 247–252.
- American Heart Association, 2011. Heart disease and stroke statistics 2011 update: A report from the american heart association.
- American Heart Association, American College of Cardiology, Society of Nuclear Medicine, 1992. Standardization of cardiac tomographic imaging. *Circulation* 86, 338–339.
- Armour, J., Pace, J., Randall, W., 1970. Interrelationship of architecture and function of the right ventricle. *J American Journal of Physiology* 218, 174–179.
- Armour, J., Randall, W., 1970. Structural basis for cardiac function. *J American Journal of Physiology* 218, 1517–1523.
- Auger, D.A., Zhong, X., Epstein, F.H., Spottiswoode, B.S.J.J.o.C.M.R., 2012. Mapping right ventricular myocardial mechanics using 3D cine DENSE cardiovascular magnetic resonance. 14, 4.
- Berr, S.S., Roy, R.J., French, B.A., Yang, Z., Gilson, W., Kramer, C.M., Epstein, F.H., 2005. Black blood gradient echo cine magnetic resonance imaging of the mouse heart. 53, 1074–1079.
- Blyth, K.G., Groenning, B.A., Martin, T.N., Foster, J.E., Mark, P.B., Dargie, H.J., Peacock, A.J., 2005. Contrast enhanced-cardiovascular magnetic resonance imaging in patients with pulmonary hypertension. *European Heart Journal* 26, 1993–1999.
- Bravo, P.E., Luo, H.-C., Pozios, I., Zimmerman, S.L., Corona-Villalobos, C.P., Sorensen, L., Kamel, I.R., Bluemke, D.A., Wahl, R.L., Abraham, M.R., Abraham, T.P., 2016. Late gadolinium enhancement confined to the right ventricular insertion points in hypertrophic cardiomyopathy: an intermediate stage phenotype? *European heart journal cardiovascular Imaging* 17, 293–300.
- CDC, Underlying Cause of Death, 1999–2014 Request. Data are from the Multiple Cause of Death Files, 1999–2014, as compiled from data provided by the 57 vital statistics jurisdictions through the Vital Statistics Cooperative Program.
- Center for Teaching and Learning in Columbia, 2016. Mechanical Properties Of The Heart I & II.
- Cerqueira, M., 2002. Standardized myocardial segmentation and nomenclature for tomographic imaging of the heart: a statement for healthcare professionals from the Cardiac Imaging Committee of the Council on Clinical Cardiology of the American Heart Association. *Circulation* 105, 539–542.
- Chen, Y., Somji, A., Yu, X., Stelzer, J.E., 2010. Altered in vivo left ventricular torsion and principal strains in hypothyroid rats. *Am J Physiol Heart Circ Physiol* 299, H1577–H1587.
- criticalecho.com, 2017.

Derrick, G.P., Josen, M., Vogel, M., Henein, M.Y., Shinebourne, E.A., Redington, A.N., 2001. Abnormalities of right ventricular long axis function after atrial repair of transposition of the great arteries. 86, 203-206.

[en.wikipedia.org/wiki/Endocardium](http://en.wikipedia.org/wiki/Endocardium), Endocardium.

[en.wikipedia.org/wiki/File:Heart\\_diastole.png](http://en.wikipedia.org/wiki/File:Heart_diastole.png), Heart diastole.

[en.wikipedia.org/wiki/File:Heart\\_systole.svg](http://en.wikipedia.org/wiki/File:Heart_systole.svg), Heart systole.

[en.wikipedia.org/wiki/File:Wiggers\\_Diagram.png](http://en.wikipedia.org/wiki/File:Wiggers_Diagram.png), Wiggers Diagram.

[en.wikipedia.org/wiki/Ventricle\\_\(heart\)](http://en.wikipedia.org/wiki/Ventricle_(heart)), Ventricle (heart).

Eyskens, B., Weidemann, F., Kowalski, M., Bogaert, J., Dymarkowski, S., Bijmens, B., Gewillig, M., Sutherland, G., Mertens, L., 2004. Regional right and left ventricular function after the Senning operation: an ultrasonic study of strain rate and strain. *Cardiol Young* 14, 255-264.

Faro, S.H., Mohamed, F.B., 2006. Functional MRI: basic principles and clinical applications, *Spiral-Echo Planar Imaging Methods*. Springer Science & Business Media, pp. 53-54.

Fine, N.M., Chen, L., Bastiansen, P.M., Frantz, R.P., Pellikka, P.A., Oh, J.K., Kane, G.C., 2013a. Outcome Prediction by Quantitative Right Ventricular Function Assessment in 575 Subjects Evaluated for Pulmonary Hypertension. 6, 711-721.

Fine, N.M., Shah, A.A., Han, I.-Y., Yu, Y., Hsiao, J.-f., Koshino, Y., Saleh, H.K., Miller, F.A., Oh, J.K., Pellikka, P.A., Villarraga, H.R.J.T.I.J.o.C.I., 2013b. Left and right ventricular strain and strain rate measurement in normal adults using velocity vector imaging: an assessment of reference values and intersystem agreement. 29, 571-580.

Fomovsky, G.M., Holmes, J.W.J.A.J.o.P.-H., Physiology, C., 2009. Evolution of scar structure, mechanics, and ventricular function after myocardial infarction in the rat. 298, H221-H228.

Ford, E.S., Ajani, U.A., Croft, J.B., Critchley, J.A., Labarthe, D.R., Kottke, T.E., Giles, W.H., Capewell, S., 2007. Explaining the decrease in U.S. deaths from coronary disease, 1980–2000. *N Engl J Med*.

Gilliam, A.D., Suever, J.D., contributors, 2016. DENSEanalysis.

Goldman, S., Raya, T.E.J.J.o.c.f., 1995. Rat infarct model of myocardial infarction and heart failure. 1, 169-177.

Grieve, D.J., Cave, A.C., Byrne, J.A., Layland, J., Shah, A.M., 2004. Analysis of ex vivo left ventricular pressure-volume relations in the isolated murine ejecting heart. *Exp Physiol* 89, 573-582.

Haber, I., Metaxas, D.N., Axel, L., 2000. Three-dimensional motion reconstruction and analysis of the right ventricle using tagged MRI. *Medical Image Analysis* 4, 335-355.

Haggerty, C.M., Kramer, S.P., Binkley, C.M., Powell, D.K., Mattingly, A.C., Charnigo, R., Epstein, F.H., Fornwalt, B.K., 2013a. Reproducibility of cine displacement encoding with stimulated echoes (DENSE) cardiovascular magnetic resonance for measuring left

ventricular strains, torsion, and synchrony in mice. *Journal of Cardiovascular Magnetic Resonance* 15, 71.

Haggerty, C.M., Kramer, S.P., Binkley, C.M., Powell, D.K., Mattingly, A.C., Charnigo, R., Epstein, F.H., Fornwalt, B.K.J.J.o.c.m.r., 2013b. Reproducibility of cine displacement encoding with stimulated echoes (DENSE) cardiovascular magnetic resonance for measuring left ventricular strains, torsion, and synchrony in mice. 15, 71.

Haggerty, C.M., Kramer, S.P., Skrinjar, O., Binkley, C.M., Powell, D.K., Mattingly, A.C., Epstein, F.H., Fornwalt, B.K., 2014. Quantification of left ventricular volumes, mass, and ejection fraction using cine displacement encoding with stimulated echoes (DENSE) MRI. *Journal of magnetic resonance imaging : JMRI* 40, 398-406.

Hamdan, A., Thouet, T., Sebastian, K., Paetsch, I., Gebker, R., Wellnhofer, E., Schnackenburg, B., Fahmy, A.S., Osman, N.F., Fleck, E., 2008. Regional right ventricular function and timing of contraction in healthy volunteers evaluated by strain-encoded MRI. 28, 1379-1385.

Hardy, R.L., 1990. Theory and applications of the multiquadric-biharmonic method 20 years of discovery 1968–1988. *Computers & Mathematics with Applications* 19, 163-208.

Hess, A.T., Zhong, X., Spottiswoode, B.S., Epstein, F.H., Meintjes, E.M., 2009. Myocardial 3D strain calculation by combining cine DENSE and cine SENC imaging. *Magn Reson Med* 62, 77–84.

Hurst, J.W., 1988. *Atlas of the Heart*. McGraw-Hill Companies.

Karliner, J.S., LeWinter, M.M., Mahler, F., Engler, R., O'Rourke, R.A., 1977. Pharmacologic and hemodynamic influences on the rate of isovolumic left ventricular relaxation in the normal conscious dog. *J Clin Invest* 60, 511-521.

Labinsky, N., Csiszar, A., Wu, J.M., Ballabh, P., Mathew, R., Podlutzky, A., Wolin, M.S., Ungvari, Z., 2008. Resveratrol Prevents Monocrotaline-induced Pulmonary Hypertension in Rats. 22, 1209.1203-1209.1203.

Li, W., Yu, X., 2010. Quantification of Myocardial Strain at Early Systole in Mouse Heart: Restoration of Undeformed Tagging Grid with Single-Point HARP. *J Magn Reson Imaging* 32, 608–614.

Liu, W., Chen, J., Ji, S., Allen, J.S., Bayly, P.V., Wickline, S.A., Yu, X., 2004. HARP MRI Tagging for Direct Quantification of Lagrangian Strain in Rat Hearts After Myocardial Infarction. *J Biomech Eng* 126, 523–528.

Liu, Z.-Q., 2018. DENSE3D\_Plugin\_4CrescentOrgan.

Lollert, A., Emrich, T., Eichstädt, J., Kampmann, C., Abu-Tair, T., Turial, S., Düber, C., Kreitner, K.-F., Staatz, G., 2018. Differences in myocardial strain between pectus excavatum patients and healthy subjects assessed by cardiac MRI: a pilot study. *European Radiology* 28, 1276-1284.

- Matsukubo, H., Matsuura, T., Endo, N., Asayama, J., Watanabe, T., 1977. Echocardiographic measurement of right ventricular wall thickness. A new application of subxiphoid echocardiography. *Circulation* 56, 278-284.
- McCam, G.P., Gan, C.T., Beek, A.M., Niessen, H.W.M., Noordegraaf, A.V., van Rossum, A.C., 2007. Extent of MRI Delayed Enhancement of Myocardial Mass Is Related to Right Ventricular Dysfunction in Pulmonary Artery Hypertension. *American Journal of Roentgenology* 188, 349-355.
- Meier, G.D., Bove, A.A., Santamore, W.P., Lynch, P.R., 1980. Contractile function in canine right ventricle. *J American Journal of Physiology-Heart Circulatory Physiology* 239, H794-H804.
- Meyer, C., 1998. Echo-planar imaging: theory, technique, and application, Spiral echo-planar imaging. Springer Verlag, Berlin and Heidelberg, pp. 633–658.
- Morris, D.A., Krisper, M., Nakatani, S., Köhncke, C., Otsuji, Y., Belyavskiy, E., Radha Krishnan, A.K., Kropf, M., Osmanoglu, E., Boldt, L.-H., Blaschke, F., Edelmann, F., Haverkamp, W., Tschöpe, C., Pieske-Kraigher, E., Pieske, B., Takeuchi, M., 2017. Normal range and usefulness of right ventricular systolic strain to detect subtle right ventricular systolic abnormalities in patients with heart failure: a multicentre study. *European Heart Journal - Cardiovascular Imaging* 18, 212-223.
- Mouchaers, K.T.B., Schalij, I., Boer, M.A.d., Postmus, P.E., Hinsbergh, V.W.M.v., Amerongen, G.P.v.N., Noordegraaf, A.V., Laarse, W.J.v.d.J.T.E.r.j., 2010. Fasudil reduces monocrotaline-induced pulmonary arterial hypertension: comparison with bosentan and sildenafil. 36 4, 800-807.
- Nucifora, G., Prati, G., Vitrella, G., Allocca, G., Cukon Buttignoni, S., Muser, D., Morocutti, G., Pinamonti, B., Sinagra, G., Selvanayagam, J., Proclemer, A., 2016. Right Ventricular Strain and Dyssynchrony Assessment in Arrhythmogenic Right Ventricular Cardiomyopathy: A Cardiac Magnetic Resonance Feature-Tracking Study. *Heart, Lung and Circulation* 25, S248.
- Patten, R.D., Hall-Porter, M.R.J.C.H.F., 2009. Small animal models of heart failure: development of novel therapies, past and present. 2, 138-144.
- Pettersen, E., Helle-Valle, T., Edvardsen, T., Lindberg, H., Smith, H.-J., Smevik, B., Smiseth, O.A., Andersen, K., 2007. Contraction Pattern of the Systemic Right Ventricle Shift From Longitudinal to Circumferential Shortening and Absent Global Ventricular Torsion. *Journal of the American College of Cardiology* 49, 2450-2456.
- Polak, J.F., Holman, B.L., Wynne, J., Colucci, W.S., 1983. Right ventricular ejection fraction: An indicator of increased mortality in patients with congestive heart failure associated with coronary artery disease. *Journal of the American College of Cardiology* 2, 217-224.
- Prentice Hall, I., 2016. Bio 100: Heart Anatomy.

Robaey, W., Bektas, S., Boyne, J., van Empel, V., Uszko-Lencer, N., Knackstedt, C., Brunner-La Rocca, H.-P., 2017. Pulmonary and right ventricular dysfunction are frequently present in heart failure irrespective of left ventricular ejection fraction. *Heart Asia* 9, e010914-e010914.

Rüssel, I.K., Tecelão, S.R., Kuijer, J.P., Heethaar, R.M., Marcus, J.T., 2009. Comparison of 2D and 3D calculation of left ventricular torsion as circumferential-longitudinal shear angle using cardiovascular magnetic resonance tagging. *J Cardiovasc Magn Reson* 11, 8.

Ryan, J.J., Huston, J., Kutty, S., Hatton, N.D., Bowman, L., Tian, L., Herr, J.E., Johri, A.M., Archer, S.L., 2015. Right Ventricular Adaptation and Failure in Pulmonary Arterial Hypertension. *Canadian Journal of Cardiology* 31, 391-406.

Sachdev, A., Villarraga, H.R., Frantz, R.P., McGoon, M.D., Hsiao, J.-F., Maalouf, J.F., Ammash, N.M., McCully, R.B., Miller, F.A., Pellikka, P.A., Oh, J.K., Kane, G.C., 2011. Right Ventricular Strain for Prediction of Survival in Patients With Pulmonary Arterial Hypertension. *Chest* 139, 1299-1309.

Sanz, J., Dellegrottaglie, S., Kariisa, M., Sulica, R., Poon, M., O'Donnell, T.P., Mehta, D., Fuster, V., Rajagopalan, S., 2007. Prevalence and Correlates of Septal Delayed Contrast Enhancement in Patients With Pulmonary Hypertension†. *The American Journal of Cardiology* 100, 731-735.

Sawamura, F., Kato, M., Fujita, K., Nakazawa, T., Beardsworth, A., 2009. Tadalafil, a Long-Acting Inhibitor of PDE5, Improves Pulmonary Hemodynamics and Survival Rate of Monocrotaline-Induced Pulmonary Artery Hypertension in Rats. *Journal of Pharmacological Sciences* 111, 235-243.

Scherptong, R.W.C., Mollema, S.A., Blom, N.A., Kroft, L.J.M., de Roos, A., Vliegen, H.W., van der Wall, E.E., Bax, J.J., Holman, E.R.J.T.I.J.o.C.I., 2009. Right ventricular peak systolic longitudinal strain is a sensitive marker for right ventricular deterioration in adult patients with tetralogy of Fallot. 25, 669-676.

Schuster, A., Morton, G., Hussain, S.T., Jogiya, R., Kutty, S., Asrress, K.N., Makowski, M.R., Bigalke, B., Perera, D., Beerbaum, P., Nagel, E., 2013. The intra-observer reproducibility of cardiovascular magnetic resonance myocardial feature tracking strain assessment is independent of field strength. *European Journal of Radiology* 82, 296-301.

Shehata, M.L., Lossnitzer, D., Skrok, J., Boyce, D., Lechtzin, N., Mathai, S.C., Girgis, R.E., Osman, N., Lima, J.A.C., Bluemke, D.A., Hassoun, P.M., Vogel-Claussen, J., 2011. Myocardial delayed enhancement in pulmonary hypertension: pulmonary hemodynamics, right ventricular function, and remodeling. *AJR. American journal of roentgenology* 196, 87-94.

Sky, 2017. *The Coronary Arteries and Major Veins of the Heart (Anterior and Inferior Views)*.

Slart, R., Bax, J., Jong, R.d., 2004. Comparison of gated PET with MRI for evaluation of left ventricular function in patients with coronary artery disease. *Nucl Med* 45, 176-182.

Spottiswoode, B.S., Zhong, X., Hess, A.T., Kramer, C.M., Meintjes, E.M., Mayosi, B.M., Epstein, F.H., 2007. Tracking myocardial motion from cine DENSE images using spatiotemporal phase unwrapping and temporal fitting. *IEEE Trans Med Imaging* 26, 15-30.

Streeter, D.D., Spotnitz, H.M., Patel, D.P., Ross, J., Sonnenblick, E.H.J.C.r., 1969. Fiber orientation in the canine left ventricle during diastole and systole. 24, 339-347.

Suever, J.D., 2016. dense3D\_plugin.

Suever, J.D., Wehner, G.J., Jing, L., Powell, D.K., Hamlet, S.M., Grabau, J.D., Mojsejenko, D., Andres, K.N., Haggerty, C.M., Fornwalt, B.K., 2017. Right Ventricular Strain, Torsion, and Dyssynchrony in Healthy Subjects Using 3D Spiral Cine DENSE Magnetic Resonance Imaging. *IEEE Trans Med Imaging* 36, 1076-1085.

Sun, J.P., James, K.B., Sheng Yang, X., Solankhi, N., Shah, M.S., Arheart, K.L., Thomas, J.D., Stewart, W.J., 1997. Comparison of Mortality Rates and Progression of Left Ventricular Dysfunction in Patients With Idiopathic Dilated Cardiomyopathy and Dilated Versus Nondilated Right Ventricular Cavities. *The American Journal of Cardiology* 80, 1583-1587.

Vandsburger, M.H., French, B.A., Kramer, C.M., Zhong, X., Epstein, F.H., 2012. Displacement-encoded and manganese-enhanced cardiac MRI reveal that nNOS, not eNOS, plays a dominant role in modulating contraction and calcium influx in the mammalian heart. *Am J Physiol Heart Circ Physiol* 302, H412-419.

Vigneault, D.M., te Riele, A.S.J.M., James, C.A., Zimmerman, S.L., Selwaness, M., Murray, B., Tichnell, C., Tee, M., Noble, J.A., Calkins, H., Tandri, H., Bluemke, D.A., 2016. Right ventricular strain by MR quantitatively identifies regional dysfunction in patients with arrhythmogenic right ventricular cardiomyopathy. 43, 1132-1139.

Youssef, A., Ibrahim, E.-S.H., Korosoglou, G., Abraham, M.R., Weiss, R.G., Osman, N.F.J.J.o.C.M.R., 2008. Strain-encoding cardiovascular magnetic resonance for assessment of right-ventricular regional function. 10, 33.

Zhang, X., Liu, Z.-Q., Singh, D., Powell, D.K., Chung, C.S., Campbell, K.S., Wenk, J.F., 2018. Differential Effects of Isoproterenol on Regional Myocardial Mechanics in Rat using 3D cine DENSE Cardiovascular Magnetic Resonance. *Journal of Biomechanical Engineering*.

Zhang, X., Liu, Z.-Q., Singh, D., Wehner, G.J., Powell, D.K., Campbell, K.S., Fornwalt, B.K., Wenk, J.F., 2017. Regional quantification of myocardial mechanics in rat using 3D cine DENSE cardiovascular magnetic resonance. 30, e3733.

Zhang, Z., Sahn, D.J., Song, X., Year Right ventricular strain analysis from 3D echocardiography by using temporally diffeomorphic motion estimation. In *International Conference on Functional Imaging and Modeling of the Heart*.

- Zhong, J., Yu, X., 2010a. Strain and Torsion Quantification in Mouse Hearts under Dobutamine Stimulation using 2D Multi-Phase MR DENSE. *Magn Reson Med* 64, 1315–1322.
- Zhong, J., Yu, X., 2010b. Strain and torsion quantification in mouse hearts under dobutamine stimulation using 2D multiphase MR DENSE. *Magn Reson Med* 64, 1315–1322.
- Zhong, X., Gibberman, L.B., Spottiswoode, B.S., Gilliam, A.D., Meyer, C.H., French, B.A., Epstein, F.H.J.J.o.C.M.R., 2011. Comprehensive Cardiovascular magnetic resonance of myocardial mechanics in mice using three-dimensional cine DENSE. 13, 83.
- Zhong, X., Helm, P.A., Epstein, F.H., 2009. Balanced multipoint displacement encoding for DENSE MRI. *Magnetic resonance in medicine* 61, 981–988.
- Zhong, X., Spottiswoode, B.S., Meyer, C.H., Kramer, C.M., Epstein, F.H., 2010. Imaging three-dimensional myocardial mechanics using navigator-gated volumetric spiral cine DENSE MRI. *Magn Reson Med* 64, 1089–1097.

## **Vita**

Zhan-Qiu Liu is the creator and maintainer of the Github project, 3D Cine DENSE Magnetic Resonance Imaging (MRI) for a Crescent-Shaped Organ.

His research interests are pulse sequence and protocol development for MRI, image processing and analysis, continuum mechanics, software development, biostatistics, and finite element modeling.

He received his Bachelor of Engineering degree in Aircraft Manufacturing Engineering at Harbin Institute of Technology, China. During his undergraduate research, he proposed a 3-DOF articulating portable working platform for astronauts during their extravehicular missions. Besides, he developed a prototype of multi-freedom morphing wing activated by shape memory alloys. He was also involved in the project of development of six-wheel lunar rover with foldable rocker-bogie suspension.

He enrolled in the Department of Mechanical Engineering at University of Kentucky in the fall of 2013. At UK, he joined Professor Jonathan F. Wenk's Computational Biomechanics Laboratory in February 2015. At present, he primarily focuses on finite element modeling of biventricular mechanics, image processing, and development of programs for computer-assisted optimization of therapies.